# A Robust Multi-Grid Pressure-Based Algorithm for MultiPhase Flow at All Speeds

M. Darwish and F. Moukalled\*
American University of Beirut,
Faculty of Engineering & Architecture,
Mechanical Engineering Department,
P.O.Box 11-0236
Beirut – Lebanon

B. Sekar Air Force Research Laboratory AFRL/PRTT Wright-Patterson AFB OH 45433-7251,USA

#### **Abstract**

This paper reports on the implementation and testing, within a full non-linear multi-grid environment, of a new pressure-based algorithm for the prediction of multiphase flow at all speeds. The algorithm is part of the Mass Conservation Based Algorithms (MCBA) group in which the pressure correction equation is derived from overall mass conservation. The performance of the new method is assessed by solving a series of two-phase test problems varying from turbulent low Mach number to supersonic flows, and from very low to high fluids density ratios. Solutions are generated for several grid sizes using the single grid (SG), the prolongation grid (PG), and the full non-linear multi-grid (FMG) methods. The main outcomes of this study are: (i) a clear demonstration of the ability of the FMG method to tackle the added non-linearity of multiphase flows, which is manifested through the performance jump observed when using the non-linear multi-grid approach as compared to the SG and PG methods; (ii) the extension of the FMG method to predict turbulent multiphase flows and multiphase flows at all speeds. The convergence history plots and CPU-times presented, indicate that the FMG method is by far more efficient than the PG method, accelerating the convergence rate, for the problems solved and the grids used, over the SG method by a factor reaching a value as high as 15.

Corresponding Author. Email: memouk@aub.edu.lb

## **Nomenclature**

 $A_p^{(k)}$ ,... coefficients in the discretized equation for  $\phi^{(k)}$ .

 $B_P^{(k)}$  source term in the discretized equation for  $\phi^{(k)}$ .

 $\mathbf{B}^{(k)}$  body force per unit volume of fluid/phase k.

 $C_{\rho}^{(k)}$  coefficient equals to  $1/R^{(k)}T^{(k)}$ .

 $C_p^{(k)}$  specific heat of fluid/phase k.

 $\mathbf{D}_{P}^{(k)}[\phi^{(k)}]$  the vector form of the *D* operator.

G<sup>(k)</sup> turbulence production rate of fluid/phase k.

 $H_{\rm p}[\phi^{(k)}]$  the H operator.

 $\mathbf{H}[\mathbf{u}^{(k)}]$  the vector form of the *HP* operator.

 $I^{(k)}$  inter-phase momentum transfer.

 $\mathbf{J}_f^{(k)D}$  diffusion flux of  $\phi^{(k)}$  across cell face 'f'.

 $\mathbf{J}_f^{(k)C}$  convection flux of  $\phi^{(k)}$  across cell face 'f'.

k<sup>(k)</sup> turbulence kinetic energy of fluid/phase k.

 $M^{(k)}$  mass source per unit volume.

P pressure.

 $Pr^{(k)}$ ,  $Pr^{(k)}_t$  laminar and turbulent Prandtl number for fluid/phase k.

 $k^{(k)}$  heat generated per unit volume of fluid/phase k.

 $Q^{(k)}$  general source term of fluid/phase k.

 $r^{(k)}$  volume fraction of fluid/phase k.

**S**<sub>f</sub> surface vector.

t time.

 $T^{(k)}$  temperature of fluid/phase k.

 $U_f^{(k)}$  interface flux velocity  $(\mathbf{v}_f^{(k)}.\mathbf{S}_f)$  of fluid/phase k.

 $\mathbf{u}^{(k)}$  velocity vector of fluid/phase k.

 $u^{(k)}, v^{(k)},...$  velocity components of fluid/phase k.

x, y Cartesian coordinates.

||a,b|| the maximum of a and b.

## **Greek Symbols**

 $\rho^{(k)}$  density of fluid/phase k.

 $\epsilon^{(k)}$  turbulence dissipation rate of fluid/phase k.

 $\Gamma^{(k)}$  diffusion coefficient of fluid/phase k.

 $\Phi^{(k)}$  dissipation term in energy equation of fluid/phase k.

 $\phi^{(k)}$  general scalar quantity associated with fluid/phase k.

 $\Delta_P \left[ \phi^{(k)} \right]$  the  $\Delta$  operator.

 $\mu^{(k)}, \mu_t^{(k)}$  laminar and turbulent viscosity of fluid/phase k.

 $\Omega$  cell volume.

 $\delta t$  time step.

# **Subscripts**

f refers to control volume face f.

P refers to the P grid point.

# **Superscripts**

C refers to convection contribution.

D refers to diffusion contribution.

(k) refers to fluid/phase k.

(k) \* refers to updated value at the current iteration.

(k) or refers to values of fluid/phase k from the previous iteration.

refers to correction field of phase/fluid k.

m refers to fluid/phase m.

old refers to values from the previous time step.

### Introduction

The numerical simulation of multiphase flows is currently one of the most challenging areas in Computational Fluid Dynamics (CFD) and has garnered over the last decade the research efforts of an increasingly larger segment of the CFD community (e.g. [1-10]). While this type of flow plays a very important role in several process industries (petrochemical, food, etc.), the use of CFD for its simulation is still restricted to a *relatively small* class of problems and its full potential is yet to be realized. This situation is largely due to the inherently complicated physics of such flows, which translates into a significant increase in numerical difficulties that can be linked to a number of factors: (i) the extreme complexity of the multiphase Navier-Stokes equations (presenting for n-fluids, n-continuity and n momentum equations), (ii) the substantial increase in non-linearity due to inter-fluid mass, momentum, energy, and continuity-volume fraction couplings (on top of the pressure-velocity coupling present in single fluid flow algorithms), (iii) and the segregated nature of many of the multiphase algorithms [11-16] that cannot resolve the different couplings in an implicit manner. This has left CFD users in the industrial sector with an unenviable situation where the simulation of large industrial-type multiphase flow problems is still a rather uncertain proposition highly dependent on initial conditions, under-relaxation factors, model simplification, mesh size, in addition to many other numerical parameters.

It is the authors' view that overcoming these hurdles can be accomplished by a multi-pronged approach whereby the development of more general multi-fluid algorithms, the extensive use of parallelization, and the use of multi-grid techniques have to play essential roles. The first area has been recently the subject of a number of papers by the authors [17,18], and the reader is referred to a recent review of all-speed multiphase flow algorithms [19], that includes several sections on robustness improvement techniques as well as a set of new algorithms capable of resolving the pressure-velocity-density-volume fraction couplings.

Parallelization already plays a major role in the simulation of large single fluid flow problems, and can play a similar role in the simulation of multiphase flows. Several methods have been proposed to parallelize Navier-Stokes solvers (e.g. functional decomposition [20], domain decomposition [21,22]). The standard approach is the one in which the computational domain is decomposed into a number of smaller sub-domains that are solved in parallel with required data exchanged at specific points during the solution and assembly procedures [23-25]. This has the benefits of applying more processing power to the problem in addition to subdividing the global domain into a number of sub-domains where the standard iterative algorithms operate more efficiently.

Multi-grid techniques achieve similar feats through different means. In this case the global domain is abstracted into a series of coarser domains, where the solution is carried out more efficiently and the results injected into the finer computational domains, thus accelerating the solution procedure and yielding major improvements in both speed of convergence and **robustness** especially when dealing with highly non-linear problems [26-43].

This paper describes an extension of the Full Approximation Storage (FAS) [30,44] multigrid algorithm to a recently developed all-speed multiphase flow algorithm based on the global Mass Conservation [18] constraint. A number of implementation issues are addressed, such as the use of special inter-grid transfer operators to maintain the realizability of the solution and the special treatment of the volume fraction equation during prolongation. In order to assess the effectiveness of the FAS multiphase implementation, a series of two-phase test problems varying from subsonic low Mach number to supersonic flows, very low to high fluids density ratios, are compared using a series of computational domains. In each case the problems are solved using (i) a single grid approach (SG), (ii) a prolongation only approach (PG) whereby the solution moves in one direction starting on the coarse grid and ending on the finest grid with the solution obtained on level n used as initial guess for the solution on

level (n+1), and (iii) finally a Full Approximation Storage (FAS) multi-grid approach with a V cycle. The aim being to quantify the effect of the FAS in addressing the increased non-linearity inherent in multiphase flow problems. Convergence history and CPU time are compared for all cases.

In what follows the governing equations for a general two-phase flow system are presented followed by a description of the discretization method and the used all-speed multiphase flow algorithm. The test problems are then presented along with a detailed evaluation of their performance with the three different approaches.

# The Governing Equations

The equations governing multiphase flows are the conservation laws of mass, momentum, and energy for each individual fluid. For turbulent multi-fluid flow situations, additional sets of equations may be needed depending on the turbulence model used. These equations should be supplemented by a set of auxiliary relations. The mass, momentum, and energy equations are respectively given by:

$$\frac{\partial \left(\mathbf{r}^{(k)}\boldsymbol{\rho}^{(k)}\right)}{\partial t} + \nabla \cdot \left(\mathbf{r}^{(k)}\boldsymbol{\rho}^{(k)}\mathbf{u}^{(k)}\right) = \mathbf{r}^{(k)}\mathbf{M}^{(k)}$$
(1)

$$\frac{\partial \left(\boldsymbol{r}^{(k)}\boldsymbol{\rho}^{(k)}\boldsymbol{u}^{(k)}\right)}{\partial t} + \nabla \cdot \left(\boldsymbol{r}^{(k)}\boldsymbol{\rho}^{(k)}\boldsymbol{u}^{(k)}\boldsymbol{u}^{(k)}\right) = \nabla \cdot \left[\boldsymbol{r}^{(k)}\left(\boldsymbol{\mu}^{(k)} + \boldsymbol{\mu}_{t}^{(k)}\right)\nabla \boldsymbol{u}^{(k)}\right] + \boldsymbol{r}^{(k)}\left(-\nabla P + \boldsymbol{B}^{(k)}\right) + \boldsymbol{I}_{M}^{(k)}$$
(2)

$$\frac{\partial \left(\mathbf{r}^{(k)} \boldsymbol{\rho}^{(k)} \mathbf{T}^{(k)}\right)}{\partial t} + \nabla \cdot \left(\mathbf{r}^{(k)} \boldsymbol{\rho}^{(k)} \mathbf{u}^{(k)} \mathbf{T}^{(k)}\right) = \nabla \cdot \left[\mathbf{r}^{(k)} \left(\frac{\boldsymbol{\mu}^{(k)}}{\mathbf{P} \mathbf{r}^{(k)}} + \frac{\boldsymbol{\mu}_{t}^{(k)}}{\mathbf{P} \mathbf{r}_{t}^{(k)}}\right) \nabla \mathbf{T}^{(k)}\right] \\
+ \frac{\mathbf{r}^{(k)}}{\mathbf{c}_{p}^{(k)}} \left\{ \boldsymbol{\beta}^{(k)} \mathbf{T}^{(k)} \left[\frac{\partial \mathbf{P}}{\partial t} + \nabla \cdot \left(\mathbf{P} \mathbf{u}^{(k)}\right) - \mathbf{P} \nabla \cdot \left(\mathbf{u}^{(k)}\right)\right] + \Phi^{(k)} + \mathbf{q}^{(k)} \right\} + \frac{\mathbf{I}_{E}^{(k)}}{\mathbf{c}_{p}^{(k)}} \tag{3}$$

where the superscript k refers to the  $k^{th}$  fluid, r the volume fraction,  $\rho$  the density,  $\boldsymbol{u}$  the velocity vector,  $\mu$  and  $\mu_t$  the laminar and turbulent viscosities, Pr and Pr<sub>t</sub> the laminar and turbulent Prandtl numbers,  $\beta$  the coefficient of thermal expansion, P the pressure,  $\boldsymbol{B}$  the body force term, T the temperature,  $\boldsymbol{M}$  the mass source,  $\boldsymbol{\Phi}$  the viscous dissipation function,  $\boldsymbol{Q}$  the

internal heat generation,  $c_p$  the specific heat, and  $I_M$  and  $I_E$  the interfacial momentum and energy transfer terms.

Several flow-dependent models have been advertised for incorporating the effect of turbulence on interfacial mass, momentum, and energy transfer, which vary in complexity from simple algebraic [45] models to state-of-the-art Reynolds-stress [46] models. However, the widely used multiphase turbulence model, adopted in this work, is the two-equation k-ε model [47], in which the fluidic conservation equations governing the turbulence kinetic energy (k) and turbulence dissipation rate (ε) for the k<sup>th</sup> fluid are given by:

$$\frac{\partial \left(r^{(k)} \rho^{(k)} k^{(k)}\right)}{\partial t} + \nabla \cdot \left(r^{(k)} \rho^{(k)} \mathbf{u}^{(k)} k^{(k)}\right) = \nabla \cdot \left(r^{(k)} \frac{\mu_t^{(k)}}{\sigma_{t_k}^{(k)}} \nabla k^{(k)}\right) + r^{(k)} \rho^{(k)} \left(G^{(k)} - \varepsilon^{(k)}\right) + I_k^{(k)} \tag{4}$$

$$\frac{\partial \left(\mathbf{r}^{(k)} \boldsymbol{\rho}^{(k)} \boldsymbol{\epsilon}^{(k)}\right)}{\partial t} + \nabla \cdot \left(\mathbf{r}^{(k)} \boldsymbol{\rho}^{(k)} \mathbf{u}^{(k)} \boldsymbol{\epsilon}^{(k)}\right) = \nabla \cdot \left(\mathbf{r}^{(k)} \frac{\boldsymbol{\mu}_{t}^{(k)}}{\boldsymbol{\sigma}_{\epsilon}^{(k)}} \nabla \boldsymbol{\epsilon}^{(k)}\right) + \mathbf{r}^{(k)} \boldsymbol{\rho}^{(k)} \frac{\boldsymbol{\epsilon}^{(k)}}{\boldsymbol{k}^{(k)}} \left(\mathbf{c}_{1\epsilon} \mathbf{G}^{(k)} - \mathbf{c}_{2\epsilon} \boldsymbol{\epsilon}^{(k)}\right) + \mathbf{I}_{\epsilon}^{(k)} \tag{5}$$

where  $I_k^{(k)}$  and  $I_\epsilon^{(k)}$  represent the interfacial turbulence terms. The turbulent viscosity is calculated as:

$$\mu_t^{(k)} = C_{\mu} \frac{\left[k^{(k)}\right]^2}{\varepsilon^{(k)}} \tag{6}$$

For two-phase flows, several extensions of the k- $\epsilon$  model that are based on calculating the turbulent viscosity by solving the k and  $\epsilon$  equations for the carrier or continuous phase only have been proposed in the literature [48-53]. In a recent article, Cokljat and Ivanov [47] presented a phase coupled k- $\epsilon$  turbulence model, intended for the cases where a non-dilute secondary phase is present, in which the k- $\epsilon$  transport equations for all phases are solved. Since the method is still not well developed, the first approach in which only the k and  $\epsilon$  equations for the carrier phase are solved is adopted in this work.

The above set of differential equations has to be solved in conjunction with constraints on certain variables represented by algebraic relations. These auxiliary relations include the

equations of state, the geometric conservation equation, and the interfacial mass, momentum, energy, and turbulence energy transfers.

Physically, the geometric conservation equation is a statement indicating that the sum of volumes occupied by the different fluids,  $r^{(k)}$ , within a cell is equal to the volume of the cell containing the fluids.

$$\sum_{k} r^{(k)} = 1 \tag{7}$$

For a compressible multiphase flow, auxiliary equations of state relating density to pressure and temperature are needed. For the k<sup>th</sup> phase, such an equation can be written as:

$$\rho^{(k)} = \rho^{(k)} (P, T^{(k)})$$
(8)

Several models have been developed for computing the interfacial mass, momentum, energy, and turbulence energy transfers terms. The closures used in this work will be detailed whenever they arise while solving problems.

In order to present a complete mathematical problem, thermodynamic relations are needed and initial and boundary conditions should supplement the above equations.

### **Discretization Procedure**

If a typical representative variable associated with phase (k) is denoted by  $\phi^{(k)}$ , equations (1)-(5) can be presented via the following general fluidic equation:

$$\frac{\partial \left(\mathbf{r}^{(k)} \boldsymbol{\rho}^{(k)} \boldsymbol{\phi}^{(k)}\right)}{\partial t} + \nabla \cdot \left(\mathbf{r}^{(k)} \boldsymbol{\rho}^{(k)} \mathbf{u}^{(k)} \boldsymbol{\phi}^{(k)}\right) = \nabla \cdot \left(\mathbf{r}^{(k)} \boldsymbol{\Gamma}^{(k)} \nabla \boldsymbol{\phi}^{(k)}\right) + \mathbf{r}^{(k)} \mathbf{Q}^{(k)}$$
(9)

where the expression for  $\Gamma^{(k)}$  and  $Q^{(k)}$  can be deduced from the parent equations.

Equation (9) is integrated over a finite volume to yield:

$$\iint_{\Omega} \frac{\partial \left( r^{(k)} \rho^{(k)} \phi^{(k)} \right)}{\partial t} d\Omega + \iint_{\Omega} \nabla \cdot \left( r^{(k)} \rho^{(k)} \mathbf{u}^{(k)} \phi^{(k)} \right) d\Omega \\
= \iint_{\Omega} \nabla \cdot \left( r^{(k)} \Gamma^{(k)} \nabla \phi^{(k)} \right) d\Omega + \iint_{\Omega} r^{(k)} Q^{(k)} d\Omega \tag{10}$$

Where  $\Omega$  is the volume of the control cell (Fig. 1). Using the divergence theorem to transform the volume integral into a surface integral and then replacing the surface integral by a summation of the fluxes over the sides of the control volume, equation (10) is transformed to:

$$\frac{\partial \left(\mathbf{r}^{(k)} \boldsymbol{\rho}^{(k)} \boldsymbol{\phi}^{(k)} \Omega\right)}{\partial t} + \sum_{\mathbf{n}b=e, w, \, \mathbf{n}, \mathbf{s}, \mathbf{t}, \, \mathbf{b}} \left(\mathbf{J}_{\mathbf{n}b}^{(k)D} + \mathbf{J}_{\mathbf{n}b}^{(k)C}\right) = \mathbf{r}^{(k)} \mathbf{Q}^{(k)} \Omega \tag{11}$$

where  $\mathbf{J}_{nb}^{(k)D}$  and  $\mathbf{J}_{nb}^{(k)C}$  are the diffusive and convective fluxes, respectively. The discretization of the diffusion term is second order accurate and follows the derivations presented in [54]. For the convective terms, the High Resolution (HR) SMART [55] scheme is employed, even for the calculation of interface densities, and applied within the context of the NVSF methodology [56]. Substituting the face values by their functional relationship relating to the node values of  $\phi$ , Eq. (11) is transformed after some algebraic manipulations into the following discretized equation:

$$A_{P}^{(k)}\phi_{P}^{(k)} = \sum_{NB} A_{NB}^{(k)}\phi_{NB}^{(k)} + B_{P}^{(k)}$$
(12)

where the coefficients  $A_P^{(k)}$  and  $A_{NB}^{(k)}$  depend on the selected scheme and  $B_P^{(k)}$  is the source term of the discretized equation . In compact form, the above equation can be written as

$$\phi^{(k)} = H_{P} \left[ \phi^{(k)} \right] = \frac{\sum_{NB} A_{NB}^{(k)} \phi_{NB}^{(k)} + B_{P}^{(k)}}{A_{P}^{(k)}}$$
(13)

The discretization procedure for the momentum equation yields an algebraic equation of the form:

$$\mathbf{u}_{p}^{(k)} = \mathbf{H}_{p} \left[ \mathbf{u}^{(k)} \right] - r^{(k)} \mathbf{D}_{p}^{(k)} \nabla_{p} \left( \mathbf{P} \right)$$

$$(14)$$

On the other hand, the fluidic mass-conservation equation (Eq. (1)) can either be viewed as a phasic volume fraction equation:

$$\mathbf{r}_{\mathbf{p}}^{(k)} = \mathbf{H}_{\mathbf{p}} \left[ \mathbf{r}^{(k)} \right] \tag{15}$$

or as a the following fluidic continuity equation that is used in deriving the pressure correction equation:

$$\frac{\left(r_{p}^{(k)}\boldsymbol{\rho}_{p}^{(k)}\right) - \left(r_{p}^{(k)}\boldsymbol{\rho}_{p}^{(k)}\right)^{Old}}{\delta t}\Omega + \Delta_{p}\left[r^{(k)}\boldsymbol{\rho}^{(k)}\boldsymbol{u}^{(k)}.\boldsymbol{S}\right] = r^{(k)}\boldsymbol{N}_{\boldsymbol{T}}^{\boldsymbol{p}(k)}$$

$$\tag{16}$$

where the  $\Delta$  operator represents the following operation:

$$\Delta_{P}[\Theta] = \sum_{f=NB(P)} \Theta_{f} \tag{17}$$

### **Solution Procedure**

The number of equations describing an n-fluid flow situation are: n fluidic momentum equations, n fluidic volume fraction (or mass conservation) equations, a geometric conservation equation, and for the case of a compressible flow an additional n auxiliary pressure-density relations. Moreover, the variables involved are the n fluidic velocity vectors, the n fluidic volume fractions, the pressure field, and for a compressible flow an additional n unknown fluidic density fields. In the current work, the n momentum equations are used to calculate the n velocity fields, n-1 volume fraction (mass conservation) equations are used to calculate n-1 volume fraction fields, and the last volume fraction field calculated using the geometric conservation equation

$$r^{(n)} = 1 - \sum_{k \in \mathbb{R}} r^{(k)} \tag{18}$$

The remaining volume fraction equation can be used to calculate the pressure field that is shared by all phases. However, instead of using this last volume fraction equation, in the class of Mass Conservation Based Algorithms (MCBA) the global conservation equation is employed, i.e. the sum of the various fluidic mass conservation equations, to derive a pressure correction equation as outlined next.

#### **The Pressure Correction Equation**

To derive the pressure-correction equation, the mass conservation equations of the various phases are added to yield the global mass conservation equation given by:

$$\sum_{k} \left\{ \frac{\left( r_{p}^{(k)} \rho_{p}^{(k)} \right) - \left( r_{p}^{(k)} \rho_{p}^{(k)} \right)^{Old}}{\delta t} \Omega + \Delta_{p} \left( r_{p}^{(k)} \rho_{p}^{(k)} \mathbf{u}^{(k)} . \mathbf{S} \right) \right\} = \sum_{k} r_{p}^{(k)} \mathbf{N}_{\mathbf{r}}^{(k)} = 0$$
(19)

In the predictor stage a guessed or an estimated pressure field from the previous iteration, denoted by  $P^{\bullet}$ , is substituted into the momentum equations. The resulting velocity fields denoted by  $\mathbf{u}^{(k)^*}$  which now satisfy the momentum equations will not, in general, satisfy the mass conservation equations. Thus, corrections are needed in order to yield velocity and pressure fields that satisfy both equations. Denoting the corrections for pressure, velocity, and density by P',  $\mathbf{u}^{(k)'}$ , and  $\rho^{(k)'}$  respectively, the corrected fields are written as:

$$P = P^{\bullet} + P', \mathbf{u}^{(k)} = \mathbf{u}^{(k)^*} + \mathbf{u}^{(k)'}, \rho^{(k)} = \rho^{(k)^{\bullet}} + \rho^{(k)'}$$
(20)

Hence the equations solved in the predictor stage are:

$$\mathbf{u}_{\mathsf{p}}^{(k)*} = \mathbf{H}_{\mathsf{p}}[\mathbf{u}^{(k)*}] - r^{(k)o}\mathbf{D}_{\mathsf{p}}^{(k)}\nabla_{\mathsf{p}}P^{o} \tag{21}$$

While the final solution satisfies

$$\mathbf{u}_{P}^{(k)} = \mathbf{H}_{P}[\mathbf{u}^{(k)}] - r^{(k)}\mathbf{D}_{P}^{(k)}\nabla_{P}P \tag{22}$$

Subtracting the two equation sets ((22) and (21)) from each other yields the following equation involving the correction terms:

$$\mathbf{u}_{P}^{(k)} = \mathbf{H}_{P}[\mathbf{u}^{(k)}] - r^{(k)o}\mathbf{D}_{P}^{(k)}\nabla_{P}P'$$

$$\tag{23}$$

Moreover, the new density and velocity fields,  $\rho^{(k)}$  and  $\mathbf{u}^{(k)}$ , will satisfy the overall mass conservation equation if:

$$\sum_{k} \left\{ \frac{\left(r_{P}^{(k)o} \rho_{P}^{(k)}\right) - \left(r_{P}^{(k)} \rho_{P}^{(k)}\right)^{old}}{\delta t} \Omega + \Delta_{P} \left[r_{P}^{(k)o} \rho_{P}^{(k)} \mathbf{u}^{(k)} \cdot \mathbf{S}\right] \right\} = 0$$

$$(24)$$

Linearizing the  $(\rho^{(k)}\mathbf{u}^{(k)})$  term, one gets

$$\left(\rho^{(k)^*} + \rho^{(k)'}\right)\left(\mathbf{u}^{(k)^*} + \mathbf{u}^{(k)'}\right) = \rho^{(k)^*}\mathbf{u}^{(k)^*} + \rho^{(k)^*}\mathbf{u}^{(k)'} + \rho^{(k)'}\mathbf{u}^{(k)^*} + \rho^{(k)'}\mathbf{u}^{(k)'}$$
(25)

Substituting equations (25) and (23) into equation (24), rearranging, and replacing density correction by pressure correction, the final form of the pressure-correction equation is written as:

$$\sum_{k} \left\{ \frac{\Omega}{\delta t} r_{p}^{(k)o} C_{\rho}^{(k)} P_{p}' + \Delta_{p} \left[ r^{(k)o} U^{(k)*} C_{\rho}^{(k)} P' \right] - \Delta_{p} \left[ r^{(k)o} \rho^{(k)*} \left( r^{(k)o} \mathbf{D}^{(k)} \nabla P' \right) \mathbf{S} \right] \right\} \\
= -\sum_{k} \left\{ \frac{r_{p}^{(k)o} \rho_{p}^{(k)*} - \left( r_{p}^{(k)} \rho_{p}^{(k)} \right)^{old}}{\delta t} \Omega + \Delta_{p} \left[ r^{(k)o} \rho^{(k)*} U^{(k)*} \right] \right\}$$
(26)

The corrections are then applied to the velocity, pressure, and density fields using the following equations:

$$\mathbf{u}_{P}^{(k)*} = \mathbf{u}_{P}^{(k)\bullet} - r^{(k)\bullet} \mathbf{D}_{P}^{(k)} \nabla_{P} P', \ P' = P^{\bullet} + P', \ \rho^{(k)*} = \rho^{(k)\bullet} + C_{\rho}^{(k)} P'$$
(27)

Numerical experiments using the above approach to simulate air-water flows have shown poor conservation of the lighter fluid. This problem can be considerably alleviated by normalizing the individual continuity equations, and hence the global mass conservation equation, by means of a weighting factor such as a reference density  $\varrho^{(k)}$  (which is fluid dependent). This approach has been adopted in solving all problems presented in this work (see [19] for details).

#### The MCBA-SIMPLE Algorithm

The overall solution procedure is an extension of the single-phase SIMPLE algorithm into multiphase flows. Since the pressure correction equation is derived from overall mass conservation, it is denoted by MCBA-SIMPLE [19]. The sequence of events in the MCBA-SIMPLE is as follows:

- 1. Solve the fluidic momentum equations for velocities.
- 2. Solve the pressure correction equation based on global mass conservation.
- 3. Correct velocities, densities, and pressure.
- 4. Solve the fluidic mass conservation equations for volume fractions.
- 5. Solve the fluidic scalar equations  $(k, \varepsilon, T, etc...)$ .
- 6. Return to the first step and repeat until convergence.

# The Multi-Grid Strategy

Similar to other iterative methods, the rate of convergence of the solution method described above does not scale linearly with the grid size, rather the convergence rate decreases more drastically as the number of grid points increases. This behavior is attributed to the speed at which the iterative solver transports the boundary information across the domain (i.e. with SOR one grid point per iteration). Since information has to travel back and forth several times to achieve convergence, acceleration of the outer iterations through the use of multigrid methods is essential for large grids. The idea underlying the multi-grid strategy is to use progressively coarser grids to accelerate the convergence rate. In mathematical terms the low-frequency error components in the finest grid appear on coarser grids as high-frequency Fourier mode that can be resolved efficiently by iterative relaxation solvers. In the present work, this strategy is adopted to accelerate convergence and thereby reduce the overall computational cost. The method used is the FMG-FAS method [44]. For a review of Multigrid methods the reader is referred, among others, to [30,44], therefore it is sufficient here to give a general description of the method used.

The multi-grid algorithm adopted in this work can be summarized as follows. Starting with the fine mesh, the coarser grid cells are generated through agglomeration of four finer grid cells, two in each direction. On the other hand, if a finer grid is required, subdividing the coarser grid control volume into four control volumes, again two in each, generates its control volumes. With the FMG cycle, the algorithm starts at the coarsest level, where the solution is first computed; this solution is interpolated onto the next finer mesh, where it is used as initial guess. This stage is called the prolongation stage (see Fig. 2a). Then iterations are performed on the fine mesh and the solution is transferred back to the coarser mesh by applying a restriction operator. In order to obtain the same approximation on each level, a forcing term is added to the discrete conservation equations on the coarser grid. This term

represents the truncation error on the coarse grid with respect to the fine grid. After performing a number of iterations on the coarse mesh, the solution is transferred back to the finer mesh in the form of a correction and a number of iterations are performed on the finer grid to smooth the fields. This process is continued until a converged solution on the fine mesh is obtained (see Fig. 2b). Then the solution is extrapolated into a finer mesh and the process repeated until convergence is reached on the desired finest mesh. This strategy has been applied to both incompressible and compressible supersonic multiphase flows and great savings have been realized as will be shown in the results section.

In the restriction step the coarse grid variables are computed from the fine grid values as:

$$\widetilde{\boldsymbol{\phi}}_{C} = \frac{1}{4} \sum_{i=1,4} \left( \boldsymbol{\phi}_{F_{i}} + \nabla \boldsymbol{\phi}_{F_{i}} \cdot \boldsymbol{d}_{F_{i}C} \right)$$
(28)

while in the prolongation step the fine grid corrections are computed from the coarse grid values as

$$\phi'_{F_i} = \phi'_C + \nabla \phi'_C \cdot \mathbf{d}_{CF_i}$$
where

$$\phi_{\rm C}' = \phi_{\rm C} - \widetilde{\phi}_{\rm C} \tag{30}$$

The special character of the volume fraction and k-ε equations necessitates modification to the prolongation procedure as described next.

While extrapolating the volume fraction field from the coarse to the fine grid, the prolongation operator may yield negative volume fraction values or values that are greater than one. Such unphysical values are detrimental to the overall convergence rate and may even cause divergence. To circumvent this problem, a simple yet very effective treatment is adopted: Once the r-values are extrapolated, a check is performed to make sure they are within bounds. If any of the r-values is found to be unbounded, the r-fluidic volume fraction equation is solved starting with the interpolated values until all of the r-values are within the set bounds. Typically less than 10 iterations are needed. This treatment has been found to be

very effective and to preserve the convergence acceleration rate. The practices of solving the volume fraction equations only on the fine grid or forcing the extrapolated unbounded values to be within the set bounds or discarding corrections that result in unbounded values [30] proved to be ineffective and slowed the convergence rate considerably.

For the k- $\epsilon$  turbulence model, the treatment suggested by Cornelius et al. [57] is adopted. This approach is based on the observation that the application of wall functions to the coarse grids would lead to unphysical values because of the relatively large distance between the wall and the boundary cell center. Thus, at wall boundaries the restricted fine grid values of k and  $\epsilon$  are held constant, and hence no corrections are calculated. In order to satisfy the realizability constraint, the restricted turbulence properties and prolongated correction values are modified accordingly.

In addition to the FMG strategy, the PG approach is also tested. This approach differs from the FMG method in that the solution moves in one direction from the coarse to the fine grids with the initial guess on level n+1 obtained by interpolation from the converged solution on level n (Fig. 2(a)). As such, the acceleration over the SG method obtained with this approach is an indication of the effect of initial guess on convergence.

#### **Results and Discussion**

The performances of the above-described solution procedures are assessed in this section by presenting solutions to the following four two-dimensional two-phase flow problems: (i) turbulent incompressible bubbly flow in a pipe, (ii) turbulent incompressible air-particle flow in a pipe, (iii) compressible dilute air-particle flow over a flat plate, and (iv) inviscid transonic dusty flow in a converging-diverging nozzle. Results are presented in terms of the CPU-time needed to converge the solution to a set level and of the convergence history. Moreover, solutions are obtained for a number of grids in order to assess the merit of the SG, PG, and FMG strategies with increasing grid density. Furthermore, predictions are compared

against available experimental data and/or numerical/theoretical values. The residual of a variable  $\phi$  at the end of an outer iteration is defined as:

$$RES_{\phi}^{(k)} = \sum_{c.v} \left| A_{p} \phi_{p}^{(k)} - \sum_{\text{all p neighbours}} A_{nb} \phi_{nb}^{(k)} - B_{p}^{(k)} \right|$$
 (31)

For global mass conservation, the imbalance in mass is given by:

$$RES_{C} = \sum_{k} \sum_{c.v.} \left| \frac{\left( r_{P}^{(k)} \rho_{P}^{(k)} \right) - \left( r_{P}^{(k)} \rho_{P}^{(k)} \right)^{Old}}{\delta t} \Omega - \Delta_{P} \left[ r^{(k)} \rho^{(k)} \mathbf{u}^{(k)} \cdot \mathbf{S} \right] - r^{(k)} \mathbf{M}^{(k)} \right|$$
(32)

All residuals are normalized by their respective inlet fluxes. Computations are terminated when the maximum normalized residual of all variables, drops below a very small number  $\varepsilon_s$  (typically  $\varepsilon_s$ =10<sup>-6</sup>). For a given problem, the same value of  $\varepsilon_s$  is used with all methodologies. In all problems, the first phase represents the continuous phase (denoted by a superscript (c)), which must be fluid, and the second phase is the disperse phase (denoted by a superscript (d)), which may be solid or fluid. Unless otherwise specified the HR SMART scheme is used in all computations reported in this study. For a given problem, all results are generated starting from the same initial guess. Moreover, it should be stated that in iterative techniques, different initial guesses might require different computational efforts.

#### Problem 1:Turbulent upward bubbly flow in a pipe

Many experimental and numerical studies involving the prediction of radial phase distribution in turbulent upward air-water flow in a pipe have appeared in the literature [58-65]. These studies indicated that the lateral forces that most strongly affect the void distribution are the lateral lift force and the turbulent stresses. As such, in addition to the usual drag force, the lift force is considered as part of the interfacial force terms in the momentum equations. In the present work, the interfacial drag forces per unit volume are given by:

$$(I_{M}^{y})_{D}^{(c)} = -(I_{M}^{y})_{D}^{(d)} = 0.375 \frac{C_{D}}{r_{p}} \rho^{(c)} r^{(d)} r^{(c)} V_{slip} (v^{(d)} - v^{(c)})$$
 (34)

where  $r_p$  is the bubble radius. The drag coefficient  $C_D$  varies as a function of the bubble Reynolds and Weber numbers defined as:

$$\begin{cases} Re_{p} = 2\frac{r_{p}}{V_{l}^{(c)}}V_{slip} \\ We = 4\rho^{(c)}\frac{r_{p}^{2}}{\sigma}V_{slip} \end{cases}$$
(35)

where  $\sigma$ , the surface tension, is assigned a value of 0.072 N/m for air-water systems. The drag coefficient is computed using the following correlations [66,67]:

$$C_{\rm D} = \frac{16}{{\rm Re}_{\rm p}} \qquad \text{for } {\rm Re}_{\rm p} < 0.49$$

$$C_{\rm D} = \frac{20}{{\rm Re}_{\rm p}^{0.643}} \qquad \text{for } 0.49 < {\rm Re}_{\rm p} < 100$$

$$C_{\rm D} = \frac{6.3}{{\rm Re}_{\rm p}^{0.385}} \qquad \text{for } {\rm Re}_{\rm p} >> 100$$

$$C_{\rm D} = \frac{8}{3} \qquad \text{for } {\rm Re}_{\rm p} >> 100 \text{ and } {\rm We} > 8$$

$$C_{\rm D} = \frac{{\rm We}}{3} \qquad \text{for } {\rm Re}_{\rm p} >> 100 \text{ and } {\rm Re}_{\rm p} > 2065.1/{\rm We}^{2.6}$$

Many investigators have considered the modeling of lift forces [66-69]. Based on their work, the following expressions are employed for the calculation of the interfacial lift forces per unit volume:

$$(\mathbf{I}_{\mathrm{M}})_{\mathrm{L}}^{(c)} = -(\mathbf{I}_{\mathrm{M}})_{\mathrm{L}}^{(d)} = C_{1} \rho^{(c)} r^{(d)} (\mathbf{u}^{(d)} - \mathbf{u}^{(c)}) x (\nabla x \mathbf{u}^{(c)})$$

$$(37)$$

where C<sub>1</sub> is the interfacial lift coefficient calculated from:

$$C_1 = C_{1a} \left( 1 - 2.78 \left\langle 0.2, r^{(d)} \right\rangle \right)$$
 (38)

where  $\langle a, b \rangle$  denotes the minimum of a and b and  $C_{1a}$  is an empirical constant.

The effect of bubbles on the turbulent field is very important. In this work, turbulence is assumed to be a property of the continuous liquid phase (c) and is computed by solving the

following modified transport equations for the turbulent kinetic energy k and its dissipation rate  $\epsilon$  that take into account the interaction between the phases:

$$\frac{\partial \left(\mathbf{r}^{(c)}\rho^{(c)}\mathbf{k}^{(c)}\right)}{\partial t} + \nabla \cdot \left(\mathbf{r}^{(c)}\rho^{(c)}\mathbf{u}^{(c)}\mathbf{k}^{(c)}\right) = \nabla \cdot \left[\mathbf{r}^{(c)}\rho^{(c)}\left(\mathbf{v}_{1}^{(c)} + \frac{\mathbf{v}_{t}^{(c)}}{\sigma_{k}^{(c)}}\right)\nabla\mathbf{k}^{(c)}\right] + \mathbf{r}^{(c)}\rho^{(c)}\left(\mathbf{G}^{(c)} - \boldsymbol{\epsilon}^{(c)}\right) + \nabla \cdot \left[\rho^{(c)}\left(\frac{\mathbf{v}_{t}^{(c)}}{\sigma_{r}}\right)\mathbf{k}^{(c)}\nabla\mathbf{r}^{(c)}\right] + \mathbf{r}^{(c)}P_{b}$$
(39)

$$\frac{\partial \left(\mathbf{r}^{(c)}\rho^{(c)}\boldsymbol{\epsilon}^{(c)}\right)}{\partial t} + \nabla \cdot \left(\mathbf{r}^{(c)}\rho^{(c)}\mathbf{u}^{(c)}\boldsymbol{\epsilon}^{(c)}\right) = \nabla \cdot \left[\mathbf{r}^{(c)}\rho^{(c)}\left(\boldsymbol{\nu}_{1}^{(c)} + \frac{\boldsymbol{\nu}_{t}^{(c)}}{\boldsymbol{\sigma}_{\epsilon}^{(c)}}\right)\nabla\boldsymbol{\epsilon}^{(c)}\right] + \mathbf{r}^{(c)}\boldsymbol{c}_{1\epsilon}\boldsymbol{P}_{b}\frac{\boldsymbol{\epsilon}^{(c)}}{\boldsymbol{k}^{(c)}} + \\
\mathbf{r}^{(c)}\rho^{(c)}\frac{\boldsymbol{\epsilon}^{(c)}}{\boldsymbol{k}^{(c)}}\left(\mathbf{c}_{1\epsilon}\boldsymbol{G}^{(c)} - \mathbf{c}_{2\epsilon}\boldsymbol{\epsilon}^{(c)}\right) + \nabla \cdot \left[\rho^{(c)}\left(\frac{\boldsymbol{\nu}_{t}^{(c)}}{\boldsymbol{\sigma}_{r}}\right)\boldsymbol{\epsilon}^{(c)}\nabla\boldsymbol{r}^{(c)}\right] \tag{40}$$

where  $G^{(c)}$  is the well known volumetric production rate of  $k^{(c)}$  by shear forces,  $\sigma_r$  the turbulent Schmidt number for volume fractions, and  $P_b$  is the production rate of  $k^{(c)}$  by drag due to the motion of the bubbles through the liquid and is given by:

$$P_b = \frac{0.375C_bC_D\rho^{(c)}r^{(d)}r^{(c)}V_{slip}^2}{r_p} \tag{41}$$

In Eq. (41)  $C_b$  is an empirical constant representing the fraction of turbulence induced by bubbles that goes into large-scale turbulence of the liquid phase. Moreover, as suggested in [65], the flux representing the interaction between the fluctuating velocity and volume fraction is modeled via a gradient diffusion approximation and added as a source term in the continuity  $\left(\nabla . \left(\rho^{(k)} D^{(k)} \nabla r^{(k)}\right)\right)$  and momentum  $\left(\nabla . \left(\rho^{(k)} D^{(k)} \mathbf{u}^{(k)} \nabla r^{(k)}\right)\right)$  equations with the diffusion coefficient D given by:

$$D^{(k)} = \frac{V_t^{(k)}}{\sigma_r} \tag{42}$$

The turbulent viscosity of the dispersed air phase (d) is assumed to be a related that that of the continuous phase through:

$$V_t^{(d)} = \frac{V_t^{(c)}}{\sigma_c} \tag{43}$$

where  $\sigma_f$  is the turbulent Schmidt number for the interaction between the two phases. The above described turbulence model is a modified version of the one described in [65] in which the turbulent viscosities of both phases are allowed to be different in contrast to what is done in [65]. This is accomplished through the introduction of the  $\sigma_f$  parameter. As such, different diffusion coefficients (D<sup>(k)</sup>) are used for the different phases. Results are compared against the experimental data reported by Seriwaza et al [58].

In the Seriwaza et al experiment [58], the Reynolds number based on superficial liquid velocity and pipe diameter is  $8\times10^4$ , the inlet superficial gas and liquid velocities are 0.077 and 1.36 m/s, respectively, and the inlet void fraction is  $5.36\times10^{-2}$  with no slip between the incoming phases. Moreover, the bubble diameter is taken as 3 mm [65], while the fluid properties are taken as  $\rho^{(c)}=1000$  Kg/m³,  $\rho^{(d)}=1.23$  Kg/m³, and  $v_1^{(c)}=10^{-6}$  m²/s. The constants in the model were set to:  $C_{1a}=0.075$ ,  $\sigma_f=0.5$ ,  $\sigma_r=0.7$ , and  $C_b=0.05$ . Predicted radial profiles of the vertical liquid velocity and void fraction presented in Fig. 3 using a grid of size 96x32 control volumes concur very well with measurements and compare favorably with numerical profiles reported by Boisson and Malin [65]. As shown, the void fraction profile indicates that gas is taken away from the pipe center towards the wall. This is caused by the lift force, which drives the bubbles towards the wall.

Having established the credibility of the physical model and numerical procedure, the next task is to compare the effects of the grid size and solution methodology on convergence and CPU time. For that purpose the calculations are performed on 5 different grids of sizes 18x3, 36x6, 72x12, 144x24, and 288x48 control volumes. On each grid, solutions are generated using the SG, PG, and FMG strategies. Results are displayed in the form of (i) the normalized residuals as a function of outer iterations (Figs. 4(a) and 4(b)), and (ii) normalized CPU time (Table 1(a)) needed for the maximum normalized residual of all variables and for both phases to drop below  $\varepsilon_s=10^{-6}$ . In Figure 4(a), the residuals of the overall mass conservation equation

and momentum equation of the carrier phase (U<sup>(c)</sup>) are presented on the finest grid for the SG, PG, and FMG methodologies. As shown, the SG method requires about 35,000 iterations to converge, whereas convergence with the PG grid method is achieved in about 10,000 iterations. Thus, a reduction ratio of 3.5 (=35,000/10,000) in the number of iterations is achieved with what amounts to simply a better initial guess. Convergence with the FMG method however requires about 1600 iterations, which represents a reduction ratio of 6.25 over the PG method and 21.9 over the SG method. The large difference between the PG and FMG is an indication of the effectiveness of the FMG method in dealing with the added nonlinearity in multiphase flows. The effect of grid size on convergence of the FMG method is depicted in Fig. 4(b). Unlike single-phase flows, the number of iterations increases with increasing grid size. This increase could be attributed to: (i) the additional coupling between the phases of the two-phase flow, which results in larger source terms (as reflected by the cyclic convergence behavior of the SG and PG methods and should be minimized by resolving the coupling in a more implicit manner (Fig. 4(a)), and (ii) the special treatment used for the k and  $\varepsilon$  equations which does not scale properly through the different grids. Nevertheless, the acceleration rate of the FMG method over the SG and PG methods increases with grid size, as can be inferred from Table 1(a) where the CPU time needed by the SG, PG, and FMG methods on all grid sizes are presented. In addition, the ratio of the time needed by the SG and PG methods to the one needed by the FMG method is displayed. This allows a direct quantitative assessment of their acceleration rate. The speed of the FMG method over the PG and SG methods is seen to increase with increasing grid density and to be about 6 and 15.7 times faster than the PG and SG methods respectively, on the finest grid.

## Problem 2:Turbulent air-particle flow in a vertical pipe

Here, the upward flow of a dilute gas-solid mixture in a vertical pipe is simulated. As in the previous problem, the axi-symmetric form of the gas and particulate transport equations are

employed. As reported in several studies [70-72], the effects of interfacial virtual mass and lift forces are small and may be neglected and the controlling interfacial force is drag (Harlow and Amsden [73]), which is given by:

$$(I_{M}^{x})_{D}^{(c)} = -(I_{M}^{x})_{D}^{(d)} = \frac{3}{8} \frac{C_{D}}{r_{D}} \rho^{(c)} r^{(d)} V_{slip} (u^{(d)} - u^{(c)})$$
(44)

$$(I_{M}^{y})_{D}^{(c)} = -(I_{M}^{y})_{D}^{(d)} = \frac{3}{8} \frac{C_{D}}{r_{D}} \rho^{(c)} r^{(d)} V_{slip} (v^{(d)} - v^{(c)})$$
 (45)

where r<sub>p</sub> represents the particle's radius, C<sub>D</sub> the drag coefficient computed from:

$$\begin{vmatrix}
C_{D} = \frac{24}{Re_{p}} & \text{for } Re_{p} < 1 \\
C_{D} = \frac{24}{Re_{p}} \left( 1 + 0.15 Re_{p}^{0.687} \right) & \text{for } 1 < Re_{p} < 1000 \\
C_{D} = 0.44 & \text{for } Re_{p} > 1000
\end{vmatrix}$$
(46)

and  $Re_p$  the Reynolds number based on the particle size as defined in Eq.(33).

As before, turbulence is assumed to be a property of the continuous gas phase (c) and is predicted using a two-phase k- $\epsilon$  model. Several extensions of the k- $\epsilon$  model for carrier-phase turbulence modulation have been proposed in the literature [48-53] and the one suggested by Chen and Wood [50], which introduces additional source terms into the turbulence transport equations, is adopted here. Thus, the turbulent viscosity is computed by solving the turbulence transport equations (Eqs. (4) and (5)) for the continuous phase with  $I_k^{(k)}$  and  $I_\epsilon^{(k)}$  evaluated using the following relations [50]:

$$I_{k}^{(c)} = -2\rho^{(d)} r^{(c)} r^{(d)} \frac{k^{(c)}}{\tau_{p}} \left( 1 - e^{-0.0825 \frac{\tau_{p}}{\tau_{e}}} \right)$$
(47)

$$I_{\varepsilon}^{(c)} = -2\rho^{(d)}r^{(c)}r^{(d)}\frac{\varepsilon^{(c)}}{\tau_{p}}$$

$$\tag{48}$$

where  $\tau_p$  and  $\tau_e$  are timescales characterizing the particle response and large-scale turbulent motion, respectively, and are computed from:

$$\begin{cases} \tau_{p} = \frac{\rho^{(d)} r^{(d)}}{F_{D}} V_{\text{slip}} \\ \tau_{e} = 0.165 \frac{k^{(c)}}{\varepsilon^{(c)}} \end{cases}$$

$$(49)$$

with  $F_D$  being the magnitude of the inter-phase drag force per unit volume. The turbulent eddy viscosity of the dispersed phase (d) is considered to be a function of that of the continuous phase and is computed using Eq. (43).

The above-described model is validated against the experimental results of Tsuji et al [70]. Results are replicated here for the case of an air Reynolds number, based on the pipe diameter (of value 30.5 mm), of  $3.3 \times 10^4$  and a mean air inlet velocity of 15.6 m/s using particles of diameter 200 µm and density  $1020 \text{ Kg/m}^3$ . In the computations, the mass-loading ratio at inlet is considered to be 1 with no slip between the phases, and  $\sigma_f$  and  $\sigma_r$  are set to 5 and  $10^{10}$ , respectively (i.e. the interaction terms included for bubbly flows are neglected here). Figure 5 shows the fully developed gas and particles mean axial velocity profiles generated using a grid of size 96x40 C.V. It is evident that there is generally a very good agreement between the predicted and experimental data with the gas velocity being slightly over predicted and the particles velocity slightly under predicted. Moreover, close to the wall, the model predictions indicate that the particles have higher velocities than the gas, which is in accord with the experimental results of Tsuji et al. [70].

Having checked the correctness of the physical model and numerical procedure, the problem is solved over five different grids of sizes 12x5, 24x10, 48x20, 96x40, and 192x80 control volumes using the SG, PG, and FMG methodologies. As in the previous problem, results are displayed in the form of (i) residual plots as a function of outer iterations (Fig. 6), and (ii) normalized CPU time (Table 1(b)) needed for the maximum normalized residuals of all variables and for all phases to drop below  $\varepsilon_s$ =10<sup>-6</sup>. In figure 6(a), residuals of the carrier phase's axial velocity (U<sup>(c)</sup>) over the densest grid using the SG, PG, and FMG methodologies

are presented. As shown (Fig. 6(a)), the performance of the PG method is poor as compared to that of the FMG method with the SG method requiring 3600 iterations, the PG method 3100 iterations (representing a reduction ratio of 1.16), and the FMG method 260 iterations (a reduction ratio of 13.85). This is another indication of the effectiveness of the FMG method in dealing with the added non-linearity of multiphase flows. The effects of grid size on convergence of the FMG method is depicted in Fig. 6(b). Again, the number of iterations needed to reach the required convergence level increases with increasing the grid size for the reasons stated earlier. The CPU times needed by the SG, PG, and FMG methods on all grid sizes in addition to the SG/FMG and PG/FMG ratios are displayed in Table 1(b). As in the previous problem, the speed of the FMG method over the PG and SG methods is seen to increase with increasing grid density and to be about 6.66 and 7.21 times faster than the PG and SG methods respectively, on the finest mesh.

#### Problem 3: Compressible dilute air-particle flow over a flat plate

As has been demonstrated in several studies [74-80], two-phase flow greatly changes the main features of the boundary layer over a flat plate. Typically, three distinct regions are defined in the two-phase boundary layer (Fig. 7(a)), based on the importance of the slip velocity between the two phases: a large-slip region close to the leading edge, a moderate-slip region further down, and a small-slip zone far downstream. The characteristic scale in this two-phase problem is the relaxation length  $\lambda_e$  [77], defined as:

$$\lambda_{e} = \frac{2}{9} \frac{\rho^{(d)} r_{p}^{2} u_{\infty}}{u^{(c)}}$$
 (50)

where  $u_{\infty}$  is the free stream velocity. The three regions are defined according to the order of magnitude of the slip parameter  $x^* = x/\lambda_e$ . In the simulation, the viscosity of the fluid is considered to be a function of temperature according to [77]:

$$\mu^{(c)} = \mu_{ref} \left( \frac{T^{(c)}}{T_{ref}} \right)^{0.6}$$
 (51)

where the reference viscosity and temperature are  $\mu_{ref}=1.86x10^{-5}$  N.s/m<sup>2</sup> and  $T_{ref}=303$  °K. Drag is the only retained interfacial force due to its dominance over other interfacial forces and is computed from [77]:

$$(I_{M}^{x})_{D}^{(c)} = -(I_{M}^{x})_{D}^{(d)} = \frac{9}{2} \frac{C_{D}}{r_{p}^{2}} r^{(d)} \mu^{(c)} (u^{(d)} - u^{(c)})$$
 (52)

$$(I_{M}^{y})_{D}^{(c)} = -(I_{M}^{y})_{D}^{(d)} = \frac{9}{2} \frac{C_{D}}{r_{p}^{2}} r^{(d)} \mu^{(c)} (v^{(d)} - v^{(c)})$$
 (53)

where the drag coefficient is given by:

$$C_{D} = \frac{1}{50} Re_{p} + \frac{7}{6} Re_{p}^{0.15}$$
 (54)

In the energy equation, heat transfer due to radiation is neglected and only convective heat transfer around an isolated particle is considered. Under such conditions, the interfacial terms in the gas (c) and particles (d) energy equations reduce to [77]:

$$I_{E}^{(c)} = Q_{g-p} + \mathbf{F}_{g-p} \cdot \mathbf{u}^{(d)}$$

$$(55)$$

$$I_{E}^{(d)} = -Q_{g-p} \tag{56}$$

where:

$$\mathbf{F}_{g-p} = \left(\mathbf{I}_{M}^{x}\right)_{D}^{(c)}\mathbf{i} + \left(\mathbf{I}_{M}^{y}\right)_{D}^{(c)}\mathbf{j}$$
(57)

$$Nu = 2.0 + 0.6 \operatorname{Re}_{p}^{\frac{1}{2}} \left( \operatorname{Pr}^{(c)} \right)^{\frac{1}{3}}$$
 (58)

$$Q_{g-p} = \frac{3}{2} \frac{r^{(d)} \lambda^{(c)} N u}{r_p^2} \left( T^{(d)} - T^{(c)} \right)$$
 (59)

In the above equations, Nu is the Nusselt number,  $Pr^{(c)}$  the gas Prandtl number,  $\lambda^{(c)}$  the gas thermal conductivity, T the temperature, and other parameters are as defined earlier.

In the simulation, the particle diameter, particle Reynolds number, material density, Prandtl number, and mass load ratio are set to:  $10 \mu m$ , 10,  $1766 \text{ kg/m}^3$ , 0.75, and 1 respectively. The wall boundary is treated as a no-slip boundary for the gas phase (i.e. both components of the gas velocity are set to zero), and as a slip boundary condition for the particles phase (i.e. the normal fluxes are set to zero). In order to bring all quantities to the same order of magnitude, results are displayed using the following dimensionless variables:

$$x^* = \frac{x}{\lambda_e}, y^* = \frac{y}{\lambda_e} \sqrt{Re}, u^* = \frac{u}{u_\infty}, v^* = \frac{v}{u_\infty} \sqrt{Re} \qquad Re = \frac{\rho u \lambda_e}{\mu}$$
 (60)

Figure 7(b) shows the results for the steady flow obtained on a rectangular domain with a

mesh of density 104x48 C.V. stretched in the y-direction. The figure provides the development of gas and particles velocity profiles within the three regions mentioned earlier. In the near leading edge area (x\*=0.1), the gas velocity is adjusted at the wall to obtain the no-slip condition as for the case of a pure gas boundary layer. The particles have no time to adjust to the local gas motion and there is a large velocity slip between the phases. In the transition region (x\*=1), significant changes in the flow properties take place. The interaction between the phases cause the particles to slow down while the gas accelerates. In the far downstream region (x\*=5), the particles have ample time to adjust to the state of the gas motion, the slip is very small, and the solution tends to equilibrium. These results are in excellent agreement with numerical solutions reported by Thevand et al. [80] (Fig. 7(b)). As in the previous tests, the problem is solved over five different grids of sizes 13x6, 26,12, 52x24, 104x48, and 208x96 control volumes using the SG, PG, and FMG methods. Results are displayed in the form of convergence history plots (Fig. 8) and normalized CPU time (Table 1(c)) with  $\varepsilon_s=10^{-6}$ . In figure 8(a), reduction with iterations of the U<sup>(c)</sup>-residuals over the densest grid (208x96 c.v.) using the SG, PG, and FMG methodologies are presented. As shown, the FMG method achieves the desired level of convergence in 430 iterations, the PG method in 2650 iterations, and the SG method in 5400 iterations. As such the iteration reduction ratios of the FMG and PG methods over the SG method are ≅12.6 and 2, respectively. This is an additional indication of the superiority of the FMG method over the PG method in dealing with the added non-linearity in compressible multiphase flows. Increasing the grid size has the same effects on the performance of the FMG method as in the previous two test problems (Fig. 8(b)). This is attributed, in addition to the added nonlinearity in multiphase flows, to the large number of parameters affecting the computations,

which are difficult to control, such as: under-relaxation factors, number of internal restriction and prolongation iterations at each level, number of algebraic solver sweeps for each dependent variable, etc.

The CPU-times for all cases considered are presented in Table 1(c). The general trend is similar to the previous cases with the SG requiring the highest CPU effort and the FMG being the most efficient on all grids. Nevertheless, the PG method is always cheaper than the SG method indicating the importance of the initial guess in iterative solvers. In fact, the use of the PG method on the dense grid accelerates the convergence rate by 513% whereas an acceleration of 949% is realized with the FMG method. Moreover, the virtues of both the FMG and PG methods increase as the grid size increases (Table 1(c)).

#### Problem 4:Inviscid transonic dusty flow in a converging-diverging nozzle

The last test considered deals with the prediction of supersonic dilute air-particle flow in an axi-symmetric converging-diverging rocket nozzle. Several researchers have analyzed the problem and data is available for comparison [81-90]. In most of the reported studies, a shorter diverging section, in comparison with the one considered here, has been used when predicting the two-phase flow. Two-phase flow results for the long configuration have only been reported by Chang et.al. [85]. The flow is assumed to be inviscid and the single-phase results are used as an initial guess for solving the two-phase problem. The physical configuration (Fig. 9(a)) is the one described in [85]. The viscosity of the fluid varies with the temperature according to Sutherland's law for air:

$$\mu^{(c)} = 1.458 \times 10^{-6} \frac{T^{(c)} \sqrt{T^{(c)}}}{T^{(c)} + 110.4}$$
(61)

The coupling between gas and particle phases is through the interfacial momentum and energy terms. The force exerted on a single particle moving through a gas is given as [86]

$$f_{x} = 6\pi r_{p} f_{D} \mu^{(c)} \left( u^{(d)} - u^{(c)} \right)$$
(62)

$$f_{y} = 6\pi r_{p} f_{D} \mu^{(c)} \left( v^{(d)} - v^{(c)} \right)$$
(63)

so that for N particles in a unit volume the effective drag force is

$$(I_{M}^{x})_{D}^{(c)} = -(I_{M}^{x})_{D}^{(d)} = \frac{9}{2} \frac{r^{(d)}}{r_{p}^{2}} f_{D} \mu^{(c)} (u^{(d)} - u^{(c)})$$
 (64)

$$(I_{M}^{y})_{D}^{(c)} = -(I_{M}^{y})_{D}^{(d)} = \frac{9}{2} \frac{r^{(d)}}{r_{p}^{2}} f_{D} \mu^{(c)} (v^{(d)} - v^{(c)})$$
 (65)

where  $f_D$  is the ratio of the drag coefficient  $C_D$  to the stokes drag  $C_{D0}$ =24/Re<sub>P</sub> and is given by [85]

$$f_{\rm D} = 1 + 0.15 \,\mathrm{Re}_{\rm p}^{0.687} + \frac{0.0175 \,\mathrm{Re}_{\rm p}}{1 + 4.25 \mathrm{x} 10^4 \,\mathrm{Re}_{\rm p}^{-1.16}} \qquad \mathrm{Re}_{\rm p} < 3 \mathrm{x} 10^5$$
 (66)

The heat transferred from gas to particle phase per unit volume is given as [86]

$$Q_{g-p} = \frac{3}{2} \frac{r^{(d)}}{r_p} \lambda^{(c)} Nu (T^{(d)} - T^{(c)})$$
(67)

Where  $\lambda^{(c)}$  is the thermal conductivity of the gas and Nu the Nusselt number, which is written as [86]

$$Nu = 2 + 0.459 Re_p^{0.55} Pr_c^{0.33}$$
(68)

The gas-particle inter-phase energy term is given by

$$I_{E}^{(c)} = \frac{9}{2} \frac{r^{(d)}}{r_{p}^{2}} f_{D} \mu^{(c)} \left( u^{(d)} - u^{(c)} \right) \mu_{d} + \frac{9}{2} \frac{r^{(d)}}{r_{p}^{2}} f_{D} \mu^{(c)} \left( v^{(d)} - v^{(c)} \right) v_{d} + \frac{3}{2} \frac{r^{(d)}}{r_{p}} \lambda^{(c)} Nu \left( T^{(d)} - T^{(c)} \right)$$
(69)

$$I_{E}^{(d)} = \frac{3}{2} \frac{r^{(d)}}{r_{p}} \lambda^{(c)} Nu \left( T^{(c)} - T^{(d)} \right)$$
 (70)

where the first two terms on the right-hand side of equation (69) represent the energy exchange due to momentum transfer.

The physical quantities employed are similar to those used in [85]. The gas stagnation temperature and pressure at inlet to the nozzle are 555 °K and  $10.34 \times 10^5$  N/m<sup>2</sup>, respectively. The specific heat for the gas and particles are  $1.07 \times 10^3$  J/Kg°K and  $1.38 \times 10^3$  J/Kg°K, respectively, and the particle density is 4004.62 kg/m<sup>3</sup>. With a zero inflow velocity angle, the fluid is accelerated from subsonic to supersonic speed in the nozzle. The inlet velocity and temperature of the particles are taken to be the same as those of the gas phase. Results for a particle of radius  $10 \, \mu m$  with a mass fraction  $\phi$ =0.3 are presented using a grid of size  $188 \times 40$ 

c.v. Figure 9(b) shows the particle volume fraction contours while Figure 9(c) displays the velocity distribution. As shown, a large particle-free zone appears due to the inability of the particles to turn around the throat corner. These findings are in excellent agreement with published results reported in [85] and others using different methodologies. A quantitative comparison of current predictions with published experimental and numerical data is presented in Fig. 10 through gas Mach number distributions along the wall (Fig. 10(a)) and centerline (Fig. 10(b)) of the nozzle for the one-phase and two-phase flow situations. As can be seen, the one-phase predictions fall on top of experimental data reported in [88-90]. Since the nozzle contour has a rapid contraction followed by a throat with a small radius of curvature, the flow near the throat wall is overturned and inclined to the downstream wall. A weak shock is thus formed to turn the flow parallel to the wall. This results in a sudden drop in the Mach number value and as depicted in Fig. 10(b), this sudden drop is correctly envisaged by the solution algorithm with the value after the shock being slightly over predicted.

Due to the unavailability of experimental data, two-phase flow predictions are compared against the numerical results reported in [85]. As displayed in Figs. 10(a) and 10(b), both solutions are in good agreement with each other indicating once more the correctness of the calculation procedures. The lower gas Mach number values in the two-phase flow is caused by the heavier particles ( $\rho^{(d)} >> \rho^{(c)}$ ), which reduce the gas velocity. Moreover, owing to the particle-free zone, the Mach number difference between the one- and two-phase flows along the wall is smaller than that at the centerline.

To compare the relative performance of the SG, PG, and FMG methodologies, the problem is solved over three different grids of sizes 47x20, 94x40, and 188x80 c.v. As before, results are displayed in the form of residual history plots (Fig. 11) and CPU times (Table 1(d)) with  $\varepsilon_s$  set to  $10^{-6}$ .

As shown in Fig. 11(a), the number of iterations required by the PG and FMG methods is relatively close with the one required by the SG method being much higher. To promote convergence with the SG method on the 188x80 grid, it was necessary to start the computations with very low under-relaxation factors. It was not possible to increase these factors until the residuals have dropped to the level shown in Fig. 11(a). Beyond that point, the higher under-relaxation factor values resulted in a fast convergence rate. In fact, the slope of the SG residual curve beyond that point, is nearly equal to the one obtained by the PG and FMG methods (Fig. 11(a)), which is a clear indication of the importance of the initial guess in supersonic flows. The proximity of performance of the PG and FMG method is due to: (i) the higher importance of initial guess in supersonic flows (as explained above), and (ii) the degradation in performance of the Multi-grid approach as the governing equations become more hyperbolic (i.e. as Mach number becomes much higher than 1, in this case it reaches a value close to 3.6) since it is best suited for elliptic equations. As in the previous problems, Fig. 11(b) indicates that the number of iterations required by the FMG method increases with increasing grid density for the reasons stated earlier.

The CPU-times presented in Table 1(d) confirm these conclusions and reveal the close performance of the PG and FMG approaches with the CPU-time needed by the FMG method being always lower. On the 94x40 grid, the FMG method is 1.31 times faster than the PG method, while it is 1.14 times faster on the densest grid. In comparison with the SG method, the FMG approach is 9 times faster on the finest mesh.

## **Closing Remarks**

This work addressed the effectiveness of the Multi-grid approach in dealing with the added non-linearity of Multiphase flows at all speeds. For that purpose the performance of the FMG method was compared against that of the SG and PG methods by solving four two-phase flow problems representing a wide variety of physical situations. Results clearly demonstrated the

robustness of the FMG method and its ability to tackle the added non-linearity of multiphase flows. Moreover, even though the rate of convergence is complex, the FMG method achieved very good reduction factors over the PG and SG methods reaching a value as high as 15.

# **Acknowledgments**

The financial support provided by the European Office of Aerospace Research and Development (EOARD) (SPC00-4071) is gratefully acknowledged.

#### References

- 1. Kunz, R. F., Cope, W. K., Venkateswaran, S.,"Development of an Implicit Method for Multi-fluid Flow Simulations," Journal of Computational Physics, Vol. 152, No. 1, June 1999, pp. 78-101
- 2. Inanc Senocak, I., and Shyy, W., "A Pressure-Based Method for Turbulent Cavitating Flow Computations," Journal of Computational Physics, Vol. 176, No. 2, Mar 2002, pp. 363-383
- 3. Jamet, D., Lebaigue, O., Coutris, N., Delhaye, J.M., "The Second Gradient Method for the Direct Numerical Simulation of Liquid-Vapor Flows with Phase Change," Journal of Computational Physics, Vol. 169, No. 2, May 2001, pp. 624-651
- 4. Jacqmin, D.,"Calculation of Two-Phase Navier-Stokes Flows Using Phase-Field Modeling," Journal of Computational Physics, Vol. 155, No. 1, Oct 1999, pp. 96-127
- 5. Gavrilyuk, S. and Saurel, R.,"Mathematical and Numerical Modeling of Two-Phase Compressible Flows with Micro-Inertia," Journal of Computational Physics, Vol. 175, No. 1, Jan 2002, pp. 326-360
- 6. Abgrall, R. and Karni, S.,"Computations of Compressible Multifluids," Journal of Computational Physics, Vol. 169, No. 2, May 2001, pp. 594-623
- 7. Vincent, S. and Caltagirone, J.P.,"A One-Cell Local Multigrid Method for Solving Unsteady Incompressible Multiphase Flows," Journal of Computational Physics, Vol. 163, No. 1, Sep 2000, pp. 172-215
- 8. Sussman, M. and Puckett, E.G., "A Coupled Level Set and Volume-of-Fluid Method for Computing 3D and Axisymmetric Incompressible Two-Phase Flows," Journal of Computational Physics, Vol. 162, No. 2, Aug 2000, pp. 301-337
- 9. Fedkiw, R.P.,"Coupling an Eulerian Fluid Calculation to a Lagrangian Solid Calculation with the Ghost Fluid Method," Journal of Computational Physics, Vol. 175, No. 1, Jan 2002, pp. 200-224
- 10. Caiden, R., Fedkiw, R.P., and Anderson, C., "A Numerical Method for Two-Phase Flow Consisting of Separate Compressible and Incompressible Regions," Journal of Computational Physics, Vol. 166, No. 1, Jan 2001, pp. 1-27
- 11. Spalding D.B., "The Calculation of Free-Convection Phenomena in Gas-Liquid Mixtures" Report HTS/76/11 Mech. Eng. Imperial College, London, 1976
- 12. Spalding, D.B., "Numerical Computation of Multi-Phase Fluid Flow and Heat Transfer", in Recent Advances in Numerical Methods in Fluid eds Taylor C., Morgan K.,, pp. 139-167, vol. 1, 1980
- 13. Spalding, D.B., "A General Purpose Computer Program for Multi-Dimensional, One and Two Phase Flow", Report HTS/81/1 Mech. Eng. Imperial College, London, 1981
- 14. Rivard, W.W. and Torrey, M.D., "KFIX: A Program for Transient Two Dimensional Two Fluid Flow", Report LA-NUREG-6623, 1978
- 15. Amsden, A.A., Harlow F.H., "KACHINA: An Eulerian Computer Program for Multifield Flows", Report LA-NUREG-5680, 1975

- 16. Amsden, A.A., Harlow F.H., "KTIFA Two-Fluid Computer Program for Down comer Flow Dynamics", Report LA-NUREG-6994, 1977
- 17. Moukalled, F. and Darwish, M." A Comparative Assessment of the Performance of Mass Conservation Based Algorithms for Incompressible Multi-Phase flows," Numerical Heat Transfer, Part B, (in print).
- 18. Moukalled, F., Darwish, M., and Sekar, B."A High Resolution Pressure-Based Algorithm for Multi-phase Flow at all Speeds," Journal of Computational Physics, (in review.
- 19. Darwish, M., Moukalled, F., and., Sekar, B." A Unified Formulation of the Segregated Class of Algorithms for Multi-Fluid Flow at All Speeds," Numerical Heat Transfer, Part B, vol.40, no. 2, pp. 99-137, 2001.
- 20. Lewis, J.A. and Brent, A.D.,"A Comparison of Coarse and Fine Grain Parallelization Strategies for the SIMPLE Pressure Correction Algorithm," In ternational Journal for Numerical Methods in Fluids, vol. 16, pp. 891-914, 1993.
- 21. Seidl, Z.V., Peric, M., and Schmidt, M., "Space- and Time-Parallel Navier-Stokes Solver for 3D Block-Adaptive Cartesian Grids," Parallel Computational Fluid Dynamics: Proc. '95 PCFD Conf., pp. 557-584, North Holland, Amsterdam, 1996.
- 22. Horton, G., "TIPSI- A Time-Parallel SIMPLE-Based Method for the Incompressible Navier-Stokes Equations," Parallel Computational Fluid Dynamics: Proc. '91 PCFD Conf., pp. 243-256, North Holland, Amsterdam, 1992.
- 23. Schafer, M., "Parallel Algorithms for the Numerical Simulation of Three-Dimensional Natural Convection," Applied Numerical Mathematics, vol. 7, pp. 347-365, 1991.
- 24. Peric, M. and Schreck, E.,"Analysis of Efficiency of Implicit CFD Methods in MIMD Computers," Parallel Computational Fluid Dynamics: Proc. '95 PCFD Conf., pp. 145-152, North Holland, Amsterdam, 1996.
- 25. Soria, M., Cadafalch, J., Consul, R., Claramunt, K., and Oliva, A.,"A parallel Algorithm for the Detailed Numerical Simulation of Reactive Flows," Parallel Computational Fluid Dynamics: Proc. '99 PCFD Conf., pp. 389-396, Amsterdam, 2000.
- 26. Durst, F. and Schafer, M.,"A Parallel Block-Structured Multigrid Method for the Prediction of Incompressible Flows," International Journal for Numerical Methods in Fluids, vol. 22, # 6, pp. 549-565, 1996.
- 27. Parsons, I. D. and Coutinho, A. L. G. A., "Finite Element Multigrid Methods for Two-Phase Immiscible Flow in Heterogeneous Media," Communications in Numerical Methods in Engineering, vol. 15, #1, pp. 1-7, 1999.
- 28. Reusken, A.,"A Multigrid Method Based on Incomplete Gaussian Elimination Numerical Linear Algebra with Applications," vol. 3, # 5, pp. 369-390, 1996.
- 29. Ecker, A. and Zulehner, W.,"On the Smoothing Property of Multigrid Methods in the Non-symmetric Case," Numerical Linear Algebra with Applications, vol. 3, #2, pp. 161-172, 1996.
- 30. Thompson, C.P. and Lezeau, P."Application of the Full Approximation Storage Method to the Numerical Simulation of Two-Dimensional Steady Incompressible Viscous Multiphase Flows," International Journal for Numerical Methods in Fluids, vol. 28, #8, pp. 1217-1239, 1998.

- 31. Favini, B., Broglia, A., and Di Mascio, A., "Multigrid Acceleration of Second-Order ENO Schemes from Low Subsonic to High Supersonic Flows," International Journal for Numerical Methods in Fluids, vol. 23, # 6, pp. 589-606, 1996.
- 32. Mavriplis, D.J. and Venkatakrishnan, V.,"A 3D Agglomeration Multigrid Solver for the Reynolds-Averaged Navier-Stokes Equations on Unstructured Meshes," International Journal for Numerical Methods in Fluids, vol. 23, #6, pp. 527-544, 1996.
- 33. Pantelelis, N.G. and Kanarachos, A.E.,"The Parallel Block Adaptive Multigrid Method for the Implicit Solution of the Euler Equations," International Journal for Numerical Methods in Fluids, vol.22, # 5, pp. 411-428, 1996.
- 34. Gjesdal, T. and Lossius, M.E.H,"Comparison of Pressure Correction Smoothers for Multigrid Solution of Incompressible Flow," International Journal for Numerical Methods in Fluids, vol. 25, #4, pp. 393-405, 1997.
- 35. Spitaleri, R.M. and Corinaldesi, L.,"A Multigrid Semi-Implicit Finite Difference Method for the Two-Dimensional Shallow Water Equations," International Journal for Numerical Methods in Fluids, vol. 25, #11, pp. 1229-1240, 1997.
- 36. Wu, J., Ritzdorf, H., Oosterlee, K., Steckel, B., and Schuller, A., "Adaptive Parallel Multigrid Solution of 2D Incompressible Navier-Stokes Equations," International Journal for Numerical Methods in Fluids, vol. 24, # 9, pp. 875-892, 1997.
- 37. Wille, S.,"Adaptive Linearization and Grid Iterations with the Tri-Tree Multigrid Refinement-Recoarsement Algorithm for The Navier-Stokes Equations," International Journal for Numerical Methods in Fluids, vol. 24, # 2, pp. 155-168, 1997.
- 38. Gerlinger, P. and Bruggemann, D., "Multigrid Convergence Acceleration for Turbulent Supersonic Flows," International Journal for Numerical Methods in Fluids, vol. 24, #10, pp. 1019-1035, 1997.
- 39. Griebel, M., Neunhoeffer, T., and Regler, H.,"Algebraic Multigrid Methods for the Solution of the Navier-Stokes Equations in Complicated Geometries," International Journal for Numerical Methods in Fluids, vol. 26, #3, pp. 281-301, 1998.
- 40. Kouatchou, J.,"A Dynamic Injection Operator in a Multigrid Solution of Convection-Diffusion Equations," International Journal for Numerical Methods in Fluids, vol. 26, # 10, pp. 1205-1216, 1998.
- 41. Böhm, M., Wechsler, K., and Schäfer, M., "A Parallel Moving Grid Multigrid Method for Flow Simulation in Rotor-Stator Configurations," International Journal for Numerical Methods in Engineering, vol. 42, #1, pp. 175-189, 1998.
- 42. Varonos, A.A. and Bergeles, G.C.,"A Multigrid Method with Higher-Order Discretization Schemes," International Journal for Numerical Methods in Fluids, vol. 35, #4, pp. 395-420, 2001.
- 43. John, V. and Tobiska, L.,"Performance of Smoothers in Coupled Multigrid Methods for the Parallel Solution of the Incompressible Navier-Stokes Equations," International Journal for Numerical Methods in Fluids, vol. 33, # 4, pp. 453-473, 2000.
- 44. Ferziger, J.H. and Peric, M., Computational Methods for Fluid Dynamics, Springer-Verlag, Berlin Heidelberg, 1996.
- 45. Baldwin, B.S. and Lomax, H.," Thin Layer Approximation and algebraic model for separated turbulent flows," AIAA Paper 78-257, 1978.

- 46. Sotiropoulos, F. and Patel, V.C., "Application of Reynolds-stress Transport Models to Stern and Wake Flow," J. Ship Res., vol. 39, p. 263, 1995.
- 47. Cokljat, D., Ivanov, V.A., Srasola, F.J., and Vasquez, S.A.,"Multiphase K-Epsilon Models for Unstructured Meshes," ASME 2000 Fluids Engineering Division Summer Meeting, June 11-15, 2000, Boston Massachusetts, USA.
- 48. Pourahmadi, F. and Humphrey, J.A.C.,"Modeling solid-fluid turbulent flows with application to predicting erosive wear," *Int. J. Phys. Chem. Hydro*, vol. 4, pp. 191-219, 1983.
- 49. Elghobashi, S.E. and Abou-Arab, T.W.,"A two-equation turbulence model for two-phase flows," Phys. Fluids, vo. 26, no. 4, pp. 931-938, 1983.
- 50. Chen, C.P. and Wood, P.E., "Turbulence closure modeling of the dilute gas-particle axisymmetric jet," A.I.C.H.E Journal, vol. 32, no. 1, pp. 163-166, 1986.
- 51. Lopez de Bertodano, M., Lee, S.J., Lahey, R.T. Jr., and Drew, D.A.,"The prediction of two-phase trubulence and phase distribution phenomena using a Reynolds stress model," ASME Journal of Fluids Engineering, vo. 112, pp. 107-113, 1990.
- 52. Lopez de Bertodano, M., Lahey, R.T. Jr., and Jones, O.C., "Development of a k-ε model for bubbly two-phase flow," ASME Journal of Fluids Engineering, vo. 116, pp. 128-134, 1994.
- 53. Lopez de Bertodano, M., Lahey, R.T. Jr., and Jones, O.C.," Phase distribution in bubbly two-phase flow in vertical ducts," Int. J. Multiphase flow, vol. 20, no. 5, pp. 805-818, 1994.
- 54. Moukalled, F. and Darwish, M.,"A Unified Formulation of the Segregated Class of Algorithms for Fluid Flow at All Speeds," Numerical Heat Transfer, Part B: Fundamentals, vol. 37, No 1, pp. 103-139, 2000.
- 55. Gaskell, P.H. and Lau, A.K.C., "Curvature compensated Convective Transport: SMART, a new boundedness preserving transport algorithm," Int. J. Num. Meth. Fluids, vol. 8, pp. 617-641, 1988.
- 56. Darwish, M.S. and Moukalled, F.," Normalized Variable and Space Formulation Methodology For High-Resolution Schemes," Numerical Heat Transfer, Part B, vol. 26, pp. 79-96, 1994.
- 57. Cornelius, C., Volgmann, W., and Stoff, H."Calculation of Three-Dimensional Turbulent Flow with a Finite Volume Multigrid Method," International Journal for Numerical Methods in Fluids, vol. 31, pp. 703-720, 1999.
- 58. Serizawa, A., Kataoka, I., and Michiyoshi, I.," Phase Distribution in Bubbly Flow," Data set No. 24, Proceedings of the Second International Workshop on Two-Phase Flow Fundamentals, Rensselaer Polytechnic Institute, Troy, NY, 1986.
- 59. Wang, S.k., Lee, S-j, Jones, Jr., O.C., and Lahey, Jr., R.T., "3-D Turbulence structure and Phase Distribution Measurements in Bubbly Two-Phase Flows," International Journal of Multiphase Flow, vol. 13, No. 3, 1987.
- 60. Antal, S.P., Lahey,R.T., and Flaherty, J.E.,"Analysis of Phase Distribution in Fully Developed Laminar Bubbly Two-Phase Flows," International Journal of Multiphase Flow, vol. 17, No. 5, pp. 635-652, 1991.
- 61. Sato, Y., sadatomi, M, and Sekoguchi, K.,"Momentum and Heat Transfer in Two-Phase Bubble flow," International Journal of Multiphase Flow, I. Theory, pp. 167-177, II. A Comparison Between Experiment and Theoretical Calculations, pp. 179-

- 190, 1981.
- 62. Lopez de Bertodano, M., Lee, S-J., Lahey, Jr., R.T., and Drew, D.A.,"The Prediction of Two-Phase Turbulence and Phase Distribution Phenomena Using a Reynolds Stress Model," Journal of Fluids Engineering, vo. 112, pp. 107-113, 1990.
- 63. Lopez de Bertodano, M., Lahey, Jr., R.T., and Jones, O.C.,"Development of a k-ε Model for Bubbly Two-Phase Flow," Journal of Fluids Engineering, vo. 116, pp. 128-134, 1994.
- 64. Nakoryakov, V.E., Kashinsky, O.N., Randin, V.V., and Timkin, L.S.,"Gas-Liquid Bubbly Flow in Vertical Pipes," Journal of Fluids Engineering, vo. 118, pp. 377-382, 1996.
- 65. Boisson, N. and Malin, M.R.,"Numerical Prediction of Two-Phase Flow in Bubble Columns," International Journal for Numerical Methods in Fluids, vol. 23, pp. 1289-1310, 1996.
- 66. Huang, B., "Modelisation Numerique D'ecoulements Diphasiques a Bulles dans les Reacteurs Chimiques," Ph.D. Thesis, Universite Claude Bernard, Lyon, 1989.
- 67. Peterson, K.O.," Etude Experimentale et Numerique des Ecoulements Diphasiques dans les Reacteurs Chimiques," Ph.D. Thesis, Universite Claude Bernard, Lyon, 1992.
- 68. Lahey, R.T., Lopez de Bertodano, M., and Jones, O.C.,"Phase Distribution in Complex Geometry Ducts," Nuclear Engineering Design, vol. 141, p. 177, 1993.
- 69. Drew, D.A. and Lahey, Jr., T.J., "The Virtual Mass and Lift Force on a Sphere in Rotating and Straining Inviscid Flow," International Journal of Multiphase Flow, vol. 13, No. 1, p. 113, 1987.
- 70. Tsuji, Y., Morikawa, Y., and Shiomi, H.,"LDV Measurements of an Air-Solid Two-Phase Flow in a Vertival Pipe," Journal of Fluid Mechanics, vo. 139, pp. 417-434, 1984.
- 71. Adeniji-Fashola, A. and Chen, C.P.,"Modeling of Confined Turbulent Fluid-Particle Flows Using Eulerian and Lagrangian Schemes,"International Journal of Heat and Mass transfer, vol.33, pp. 691-701, 1990.
- 72. Naik, S. and Bryden, I.G., "Prediction of Turbulent Gas-Solids Flow in Curved Ducts Using The Eulerian-Lagrangian Method," International Journal for Numerical Methods in Fluids, vol. 31, pp. 579-600, 1999.
- 73. Harlow, F.H. and Amsden, A.A., "Numerical Calculation of Multiphase Fluid Flow," Journal of Computational Physics, vol. 17, pp. 19-52, 1975.
- 74. Osiptsov, A.N., "Structure of the Laminar Boundary Layer of a Disperse Medium on a Flat Plate," Fluid Dyn., vol. 15, pp. 512-517, 1980.
- 75. Prabha, S. and Jain, A.C.,"On the Use of Compatibility Conditions in the Solution of Gas Particulate Boundary Layer Equations," Appl. Sci. res., vol. 36, pp. 81-91, 1980.
- 76. Sgleton, R.E.,"The Incompressible Gas Solid Particle Flows Over a Semi-Infinite Flat Plate," Z. Angew Math. Phys., vol. 19, p. 545, 1965.
- 77. Wang, B.Y., and Glass, I.I., "Compressible Laminar Boundary Layer Flows of a Dusty Gas Over a Semi-Infinite Flat Plate," Journal of Fluid Mechanics, vol. 186, pp. 223-241, 1988.

- 78. Soo, S.L.,"Boundary Layer Motion of a Gas-Solids Suspension," Proc. Symp. Interaction Between Fluids and Particles, Inst. Chem. Eng., pp. 50-63, 1962.
- 79. Chamkha, A.J., and Peddieson, J.J.R.,"Boundary Layer Flow of a Particulate Suspenson Past a Flat Plate," International Journal of Multiphase Flow, vol. 17, pp. 805-808, 1991.
- 80. Thevand, N., Daniel, E., and Loraud, J.C., "On high-Resolution Schemes for Solving Unsteady Compressible Two-Phase Dilute Viscous Flows," International Journal of Numerical Methods in Fluids, vol. 31, pp. 681-702, 1999.
- 81. Chang, I.S.,"One and Two-Phase Nozzle Flows," AIAA J., vol. 18, pp. 1455-1461, 1980
- 82. Ishii, R. and Kawasaki, K.,"Limiting Particle Streamline in the flow of a Gas-Particle Mixture Through an Axially Symmetric Nozzle," Phys. Fluids, vol. 25, No. 6, pp. 959-966, 1982.
- 1. Ishii, R., Umeda, Y., and Kawasaki, K.,"Nozzle Flows of Gas-Particle Mixtures," Phys. Fluids, vol. 30, No. 3, pp. 752-760, 1987.
- 83. Hwang, C.J. and Chang, G.C.,"Numerical Study of Gas-Particle Flow in a Solid Rocket Nozzle," AIAA Journal, vol. 26, No. 6, pp. 682-689, 1988.
- 84. Chang, H.T., Hourng, L.W., and Chien, L.E., "Application of Flux-Vector-Splitting Scheme to a Dilute Gas-Particle JPL Nozzle Flow," International Journal for Numerical Methods in Fluids, vol. 22, pp. 921-935, 1996.
- 85. Mehta, R.C. and Jayachandran, T.,"A Fast Algorithm to Solve Viscous Two-Phase Flow in an Axisymmetric Rocket Nozzle," International Journal for Numerical Methods in Fluids, vol. 26, pp. 501-517, 1998.
- 86. Igra, O., Elperin, I., and Ben-Dor, G.,"Dusty Gas Flow in a Converging-Diverging Nozzle," Journal of Fluids Engineering, vol. 121, pp. 908-913, 1999.
- 87. Back, L.H. and Cuffel, R.F., "Detection of Oblique Shocks in a Conical Nozzle with a Circular-arc Throat," AIAA Journal, vol. 4, pp. 2219-2221, 1966.
- 88. Back, L.H. Massier, P.F., and Cuffel, R.F., "Flow Phenomena and Convective Heat Transfer in a Conical Supersonic Nozzle," Journal of Spacecraft, vol. 4, pp. 1040-1047, 1967.
- 89. Cuffel, R.F., Back, L.H., and Massier, P.F.,"Transonic Flowfield in a Supersonic Nozzle with Small Throat Radius of Curvature," AIAA Journal, vol. 7, pp. 1364-1366, 1969.

## **Figure Captions**

- Fig. 1 Control volume.
- Fig. 2 (a) the prolongation only and (b) FMG strategies
- Fig. 3 Comparison of fully developed liquid velocity and void fraction profiles for Turbulent upward bubbly flow in a pipe against Seriwaza et al. data.
- Fig. 4 (a) Mass and U<sup>(c)</sup> residual history plots for the FMG, PG, and SG methods on the finest mesh for turbulent bubbly flow in a pipe; (b) U<sup>(c)</sup> residual history plots for the FMG method on the various levels for turbulent bubbly flow in a pipe.
- Fig. 5 Comparison of fully developed gas and particle velocity profiles for turbulent air-particle flow in a pipe.
- Fig. 6 (a) U<sup>(c)</sup> residual history plots for the FMG, PG, and SG methods on the finest mesh for turbulent air-particle flow in a pipe; (b) Mass residual history plots for the FMG method on the various levels for turbulent air-particle flow in a pipe.
- Fig. 7 (a) The three different regions within the boundary layer of dusty flow over a flat plate; (b) Comparison of fully developed gas and particle velocity profiles inside the boundary layer at different axial locations for dilute two-phase flow over a flat plate.
- Fig. 8 (a)  $U^{(c)}$  residual history plots for the FMG, PG, and SG methods on the finest mesh for compressible dusty flow over a flat plate; (b)  $U^{(c)}$  residual history plots for the FMG method on the various levels for compressible dusty flow over a flat plate.
- Fig. 9 (a) Physical domain for the dusty gas flow in a converging-diverging nozzle;(b) Volume Fraction contours and (c) particle velocity vectors for dusty gas flow in a converging-diverging nozzle.

- Fig. 10 Comparison of one-phase and two-phase gas Mach number distributions along the (a) wall and (b) centerline of dusty flow in a converging-diverging nozzle.
- Fig. 11 (a) Mass residual history plots for the FMG, PG, and SG methods on the finest mesh for compressible dusty flow in a converging-diverging nozzle;
  - (b) Mass residual history plots for the FMG method on the various levels for compressible dusty in a converging-diverging nozzle.

Table 1(a) CPU-times for: (a) turbulent bubbly flow in a pipe; (b) turbulent airparticle flow in a pipe; (c) compressible dusty flow over a flat plate; (d) compressible dusty flow in a converging-diverging nozzle.

(a)

Grid (c.v.)	SG	Levels	PG	FMG	PG/FMG	SG/FMG
18x3	0.73	1	0.73	0.73	1.00	1.00
36x6	4.77	2	3.82	3.63	1.05	1.31
72x12	72.75	3	34.23	25.29	1.35	2.88
144x24	876.48	4	398.33	149.52	2.66	5.86
288x48	38840.37	5	14975.97	2480.34	6.04	15.66

(b)

Grid (c.v.)	SG	Levels	PG	FMG	PG/FMG	SG/FMG
12x5	0.56	1	0.56	0.56	1.00	1.00
24x10	3.78	2	3.26	2.78	1.17	1.36
48x20	41.14	3	33.27	16.96	1.96	2.43
96x40	464.55	4	368.12	92.35	3.99	5.03
192x80	5232.38	5	4833.98	725.40	6.66	7.21

(c)

Grid (c.v.)	SG	Levels	PG	FMG	PG/FMG	SG/FMG
13x6	1.34	1	1.34	1.34	1.00	1.00
26x12	5.44	2	5.05	3.75	1.35	1.45
52x24	41.02	3	36.47	18.13	2.01	2.26
104x48	500.05	4	376.12	101.49	3.71	4.93
208x96	7738.08	5	4181.42	815.38	5.13	9.49

(d)

Grid (c.v.)	SG	Levels	PG	FMG	PG/FMG	SG/FMG
47x20	28.20	1	28.20	28.20	1.00	1.00
94x40	470.82	2	334.15	255.30	1.31	1.84
188x80	23168.56	3	2912.77	2558.71	1.14	9.05

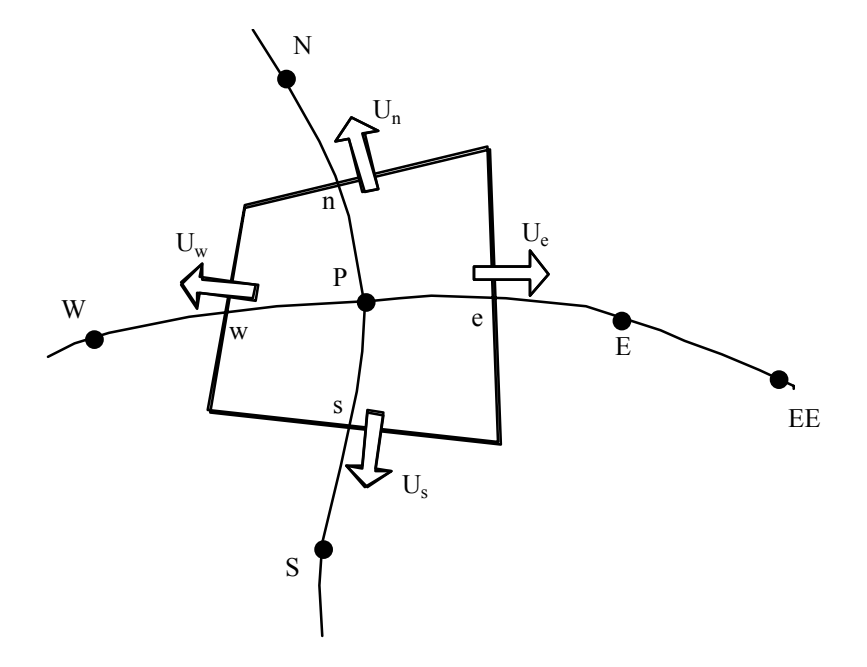


Fig. 1 Control volume.

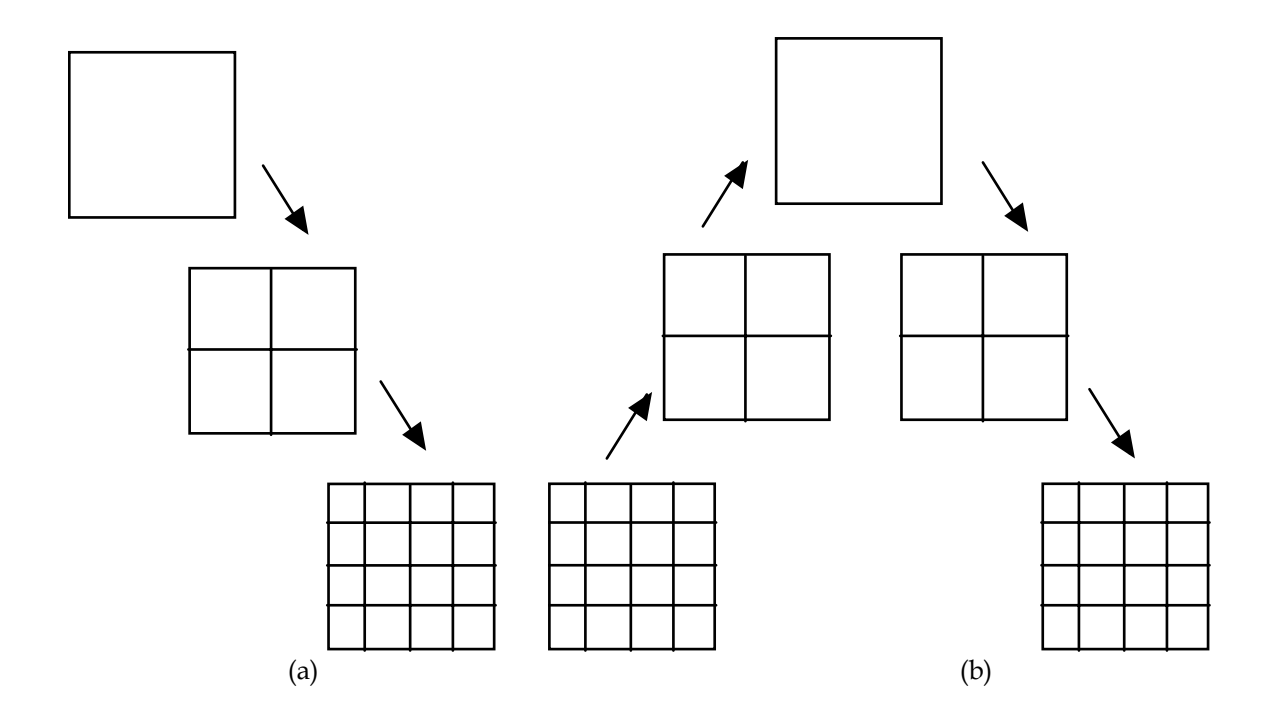


Fig. 2 (a) the prolongation only and (b) FMG strategies

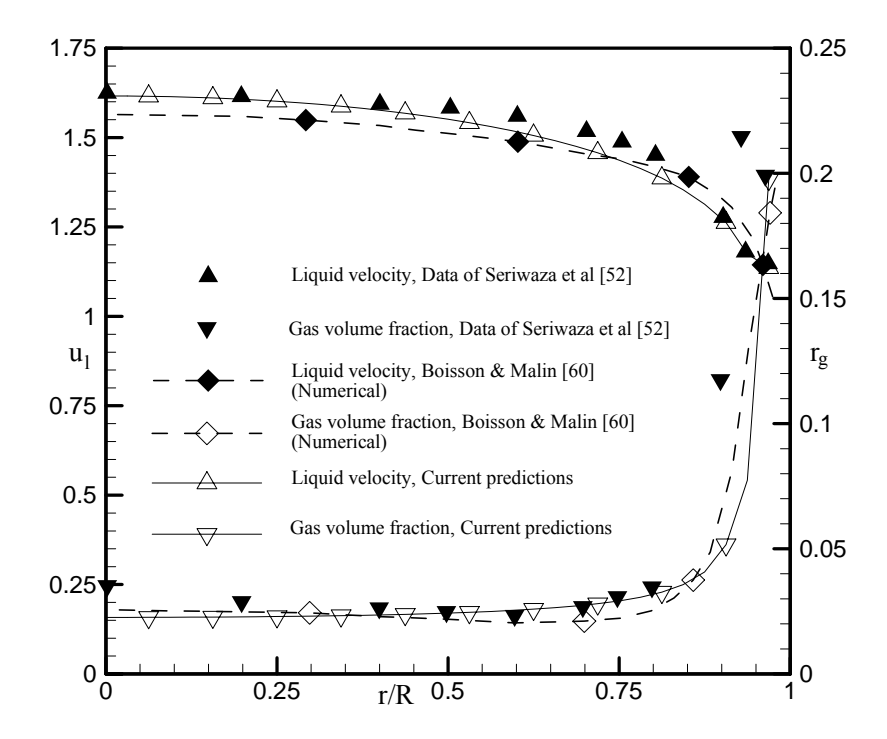


Fig. 3 Comparison of fully developed liquid velocity and void fraction profiles for Turbulent upward bubbly flow in a pipe against Seriwaza et al. data.

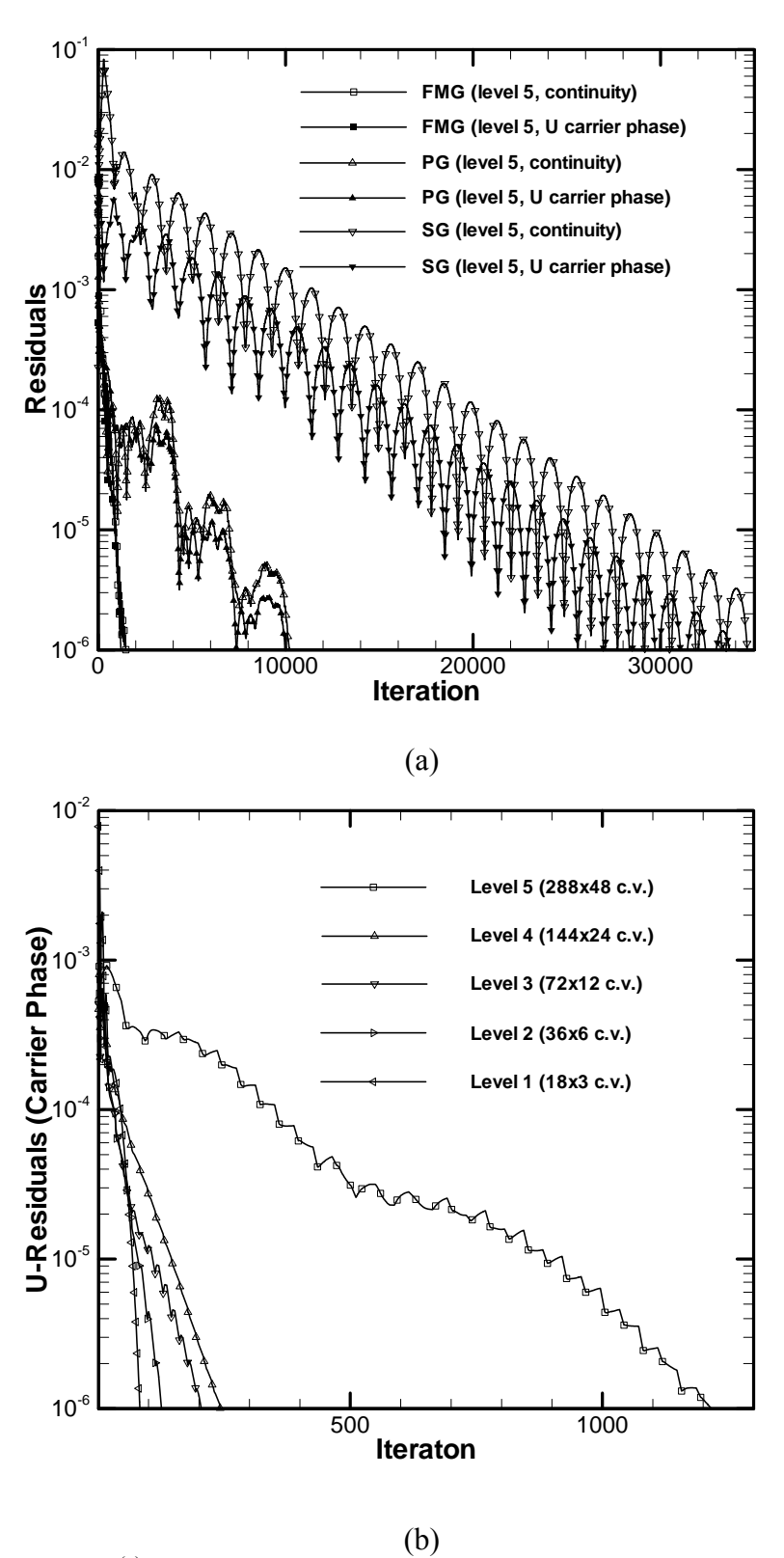


Fig. 4 (a) Mass and U<sup>(c)</sup> residual history plots for the FMG, PG, and SG methods on the finest mesh for turbulent bubbly flow in a pipe; (b) U<sup>(c)</sup> residual history plots for the FMG method on the various levels for turbulent bubbly flow in a pipe.

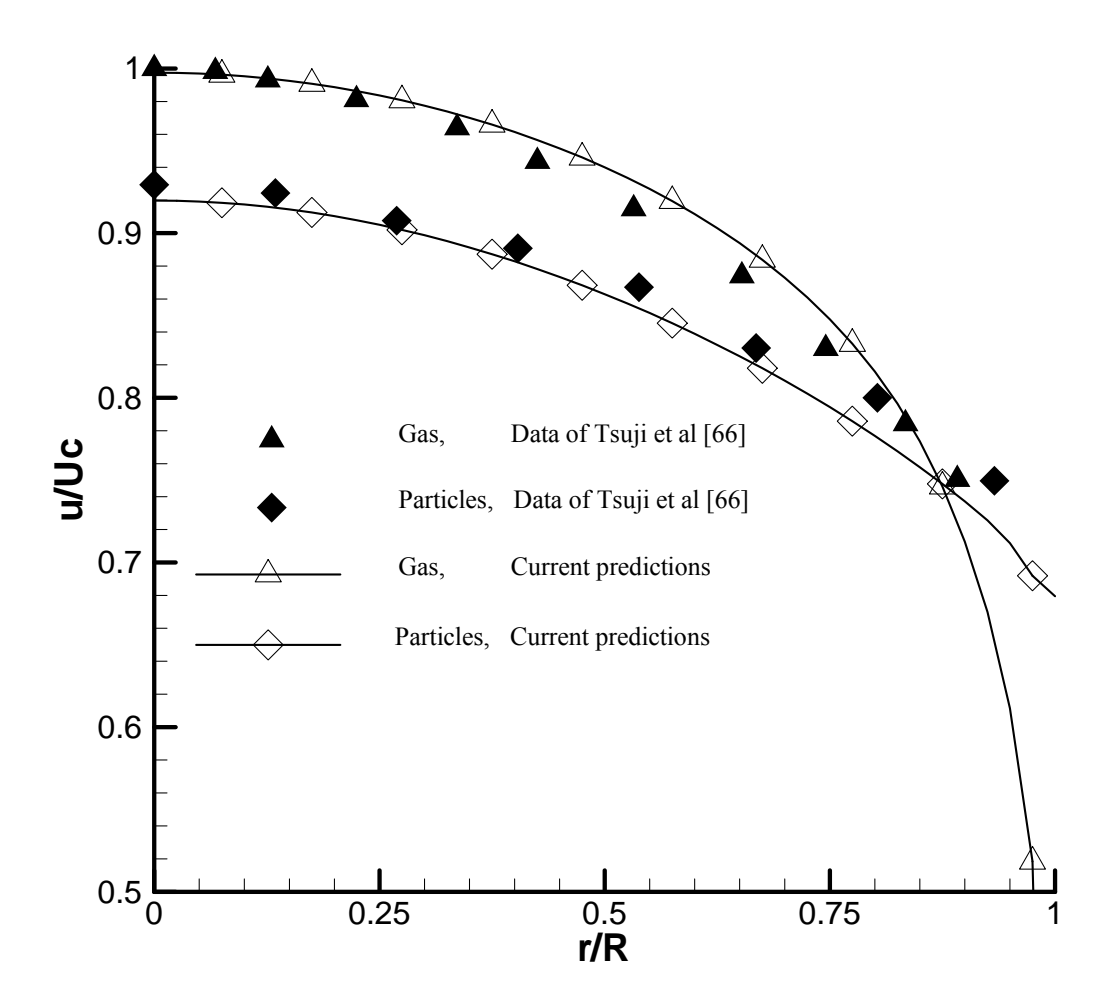
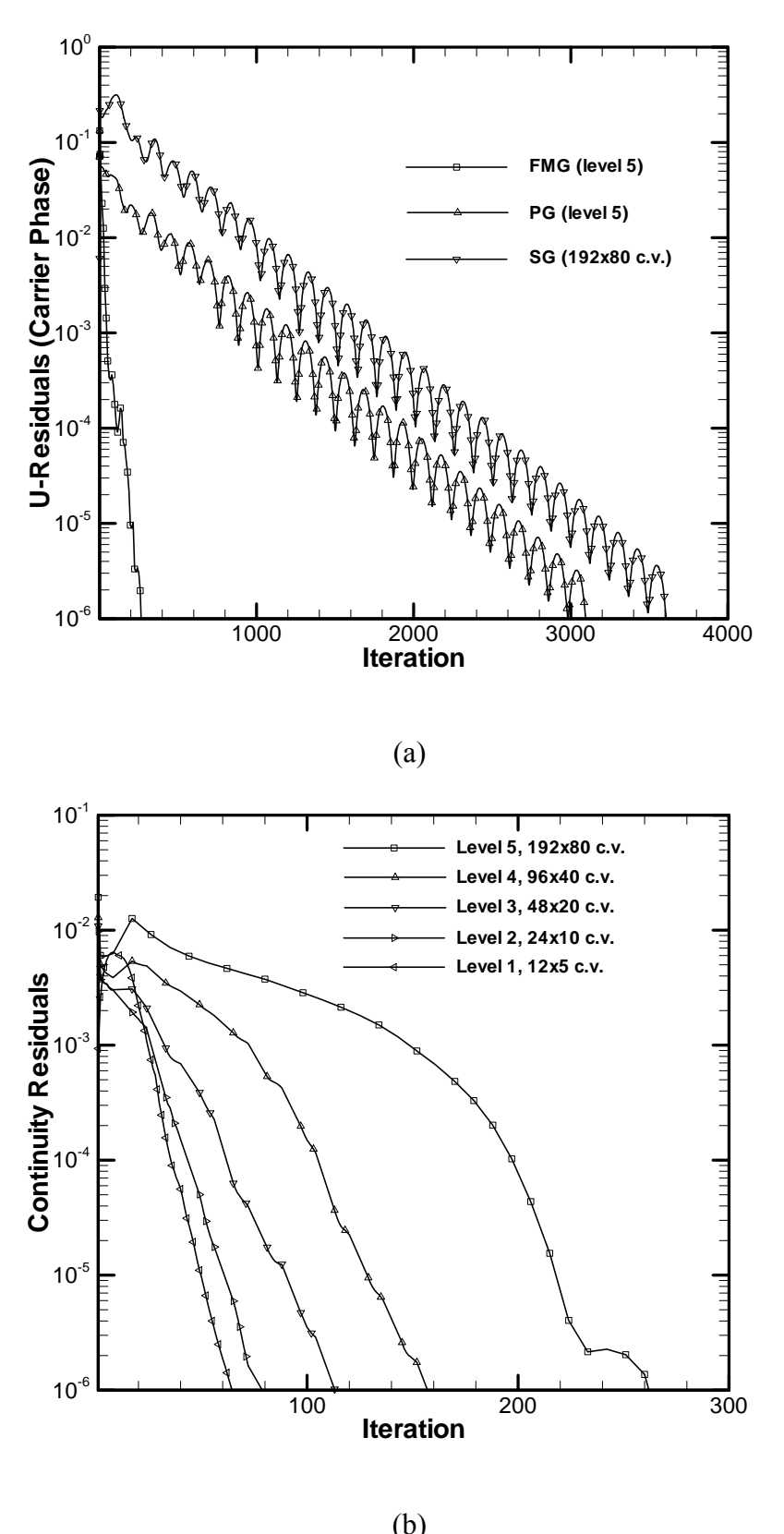
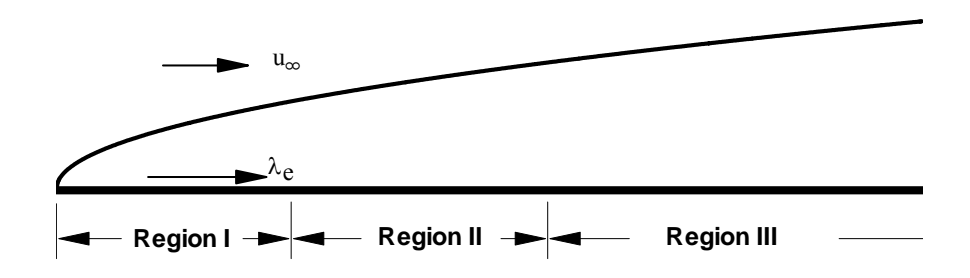


Fig. 5 Comparison of fully developed gas and particle velocity profiles for turbulent air-particle flow in a pipe.



(b)
Fig. 6 (a) U<sup>(c)</sup> residual history plots for the FMG, PG, and SG methods on the finest mesh for turbulent air-particle flow in a pipe; (b) Mass residual history plots for the FMG method on the various levels for turbulent air-particle flow in a pipe.



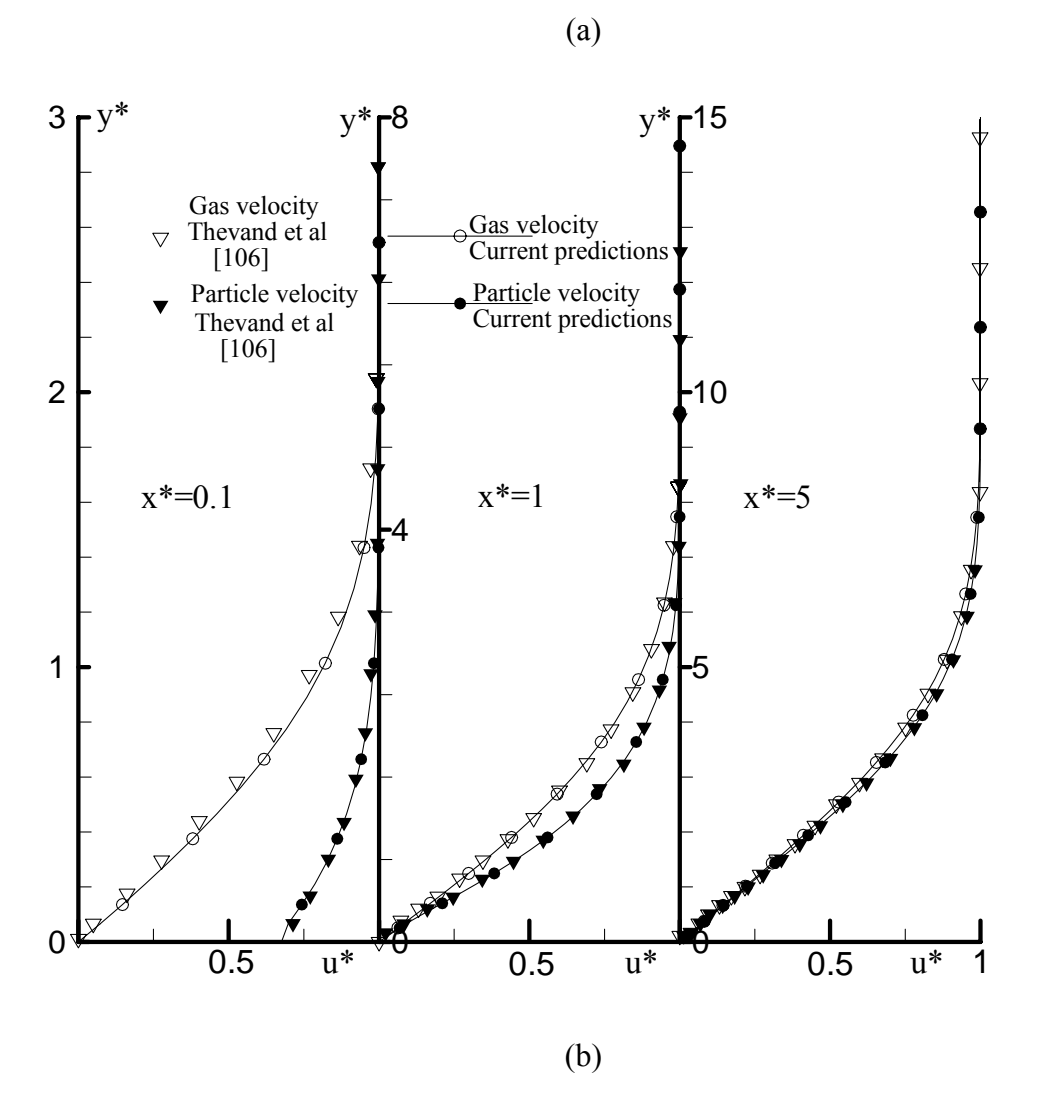


Fig. 7 (a) The three different regions within the boundary layer of dusty flow over a flat plate; (b) Comparison of fully developed gas and particle velocity profiles inside the boundary layer at different axial locations for dilute two-phase flow over a flat plate.

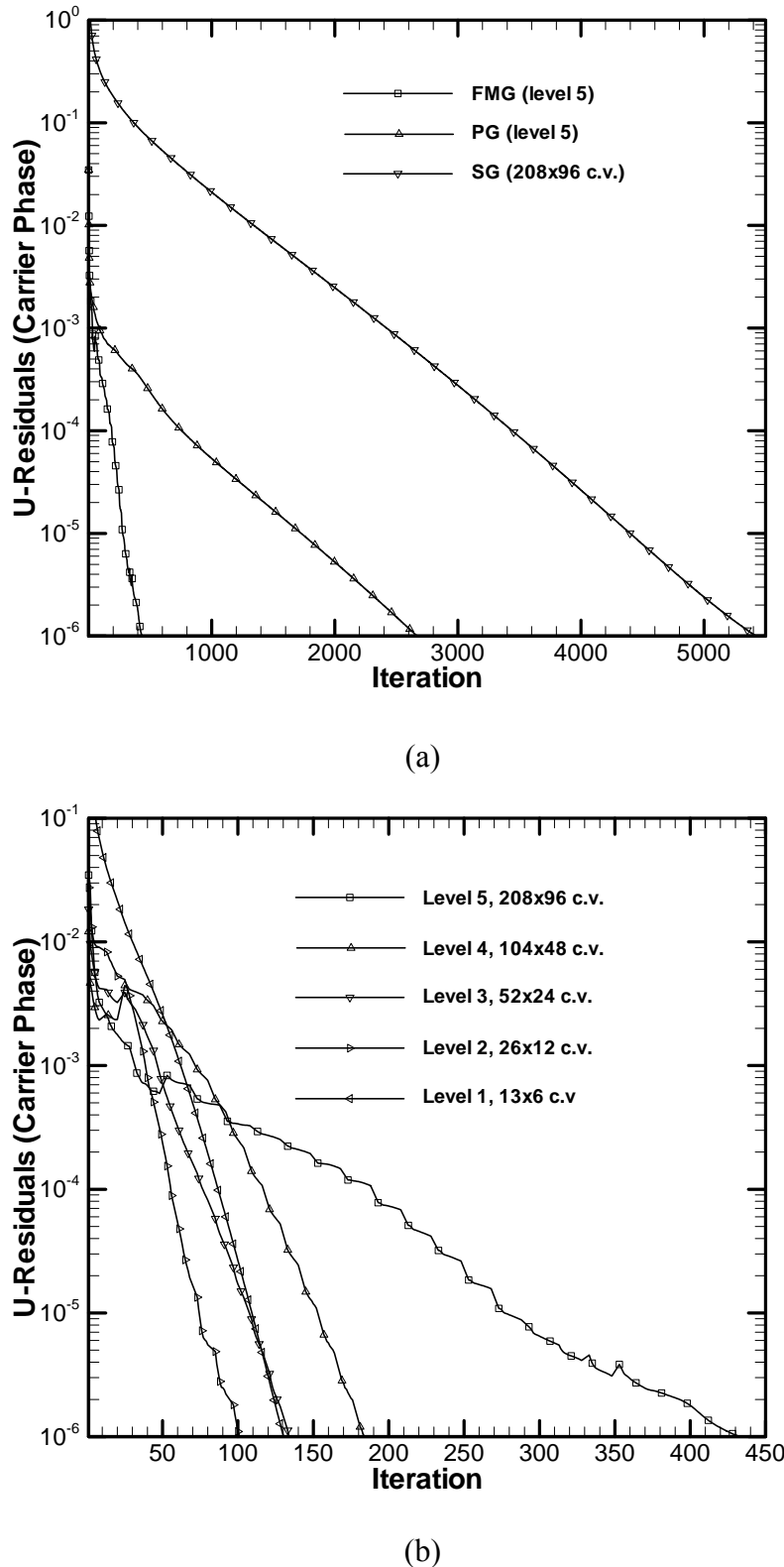


Fig. 8 (a) U<sup>(c)</sup> residual history plots for the FMG, PG, and SG methods on the finest mesh for compressible dusty flow over a flat plate; (b) U<sup>(c)</sup> residual history plots for the FMG method on the various levels for compressible dusty flow over a flat plate.

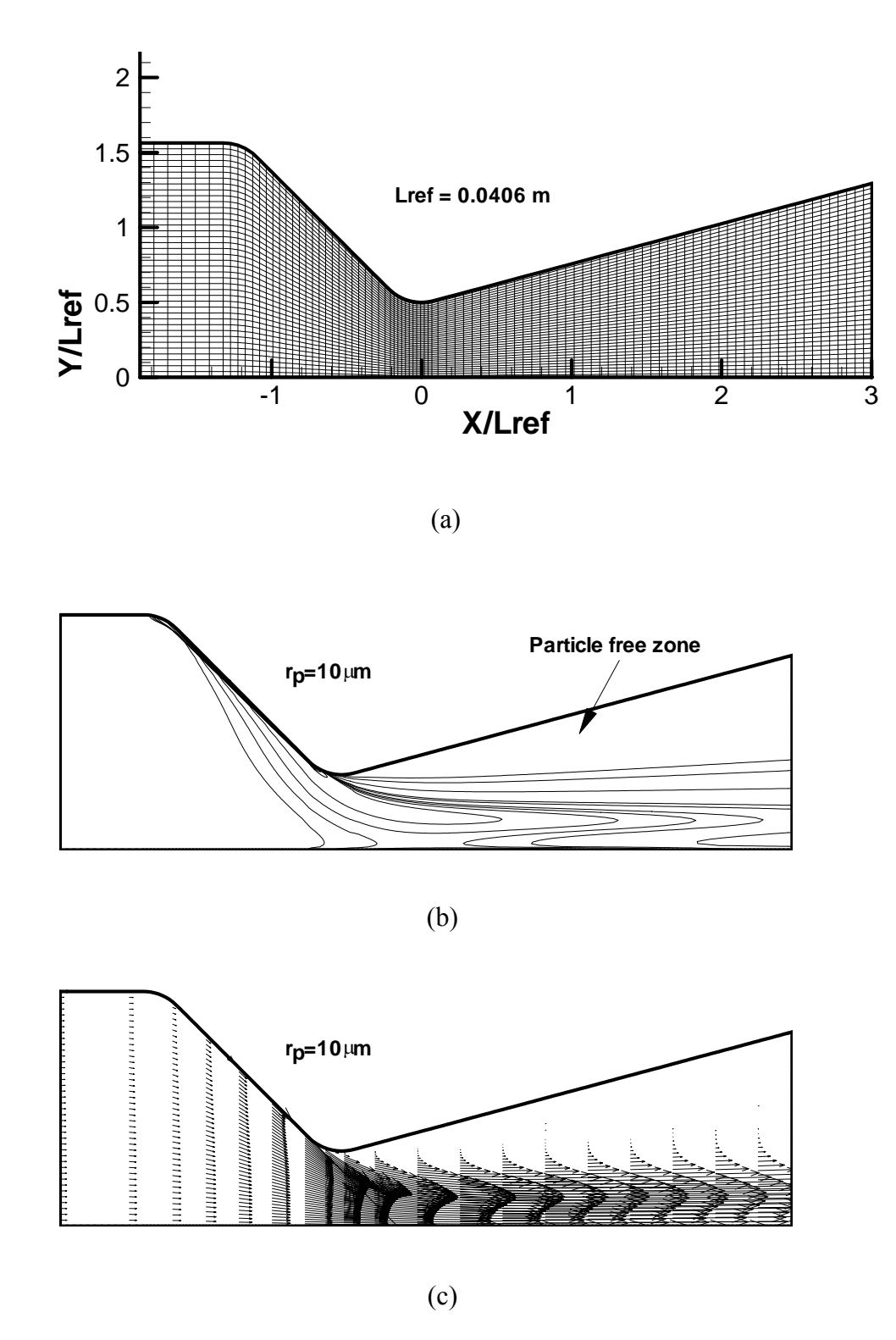
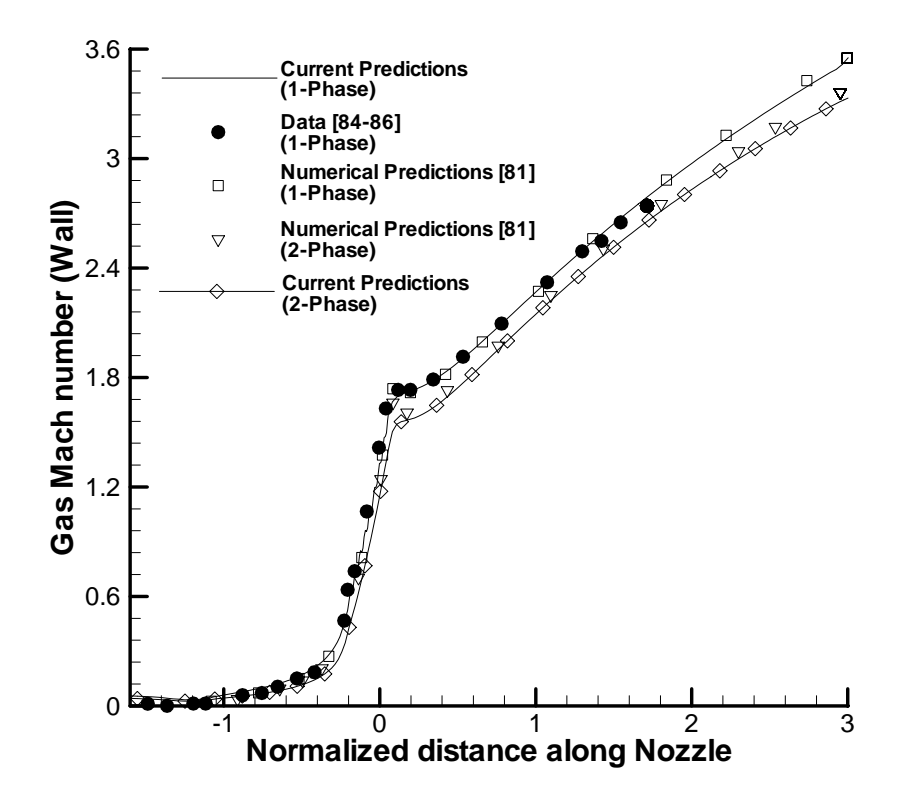
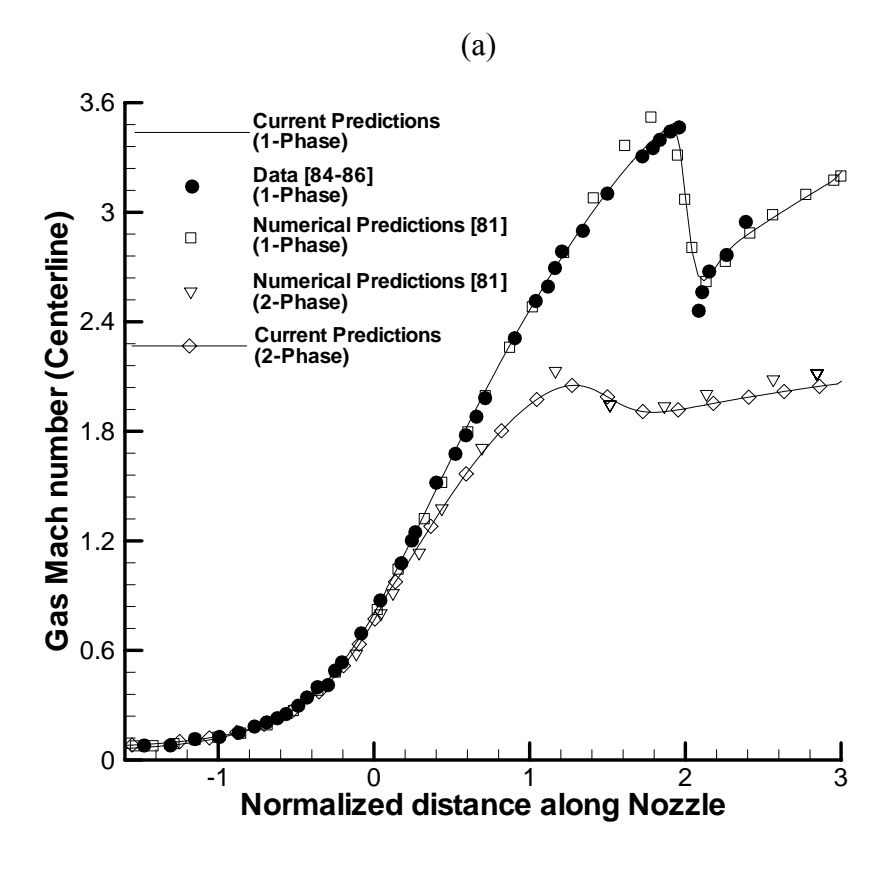


Fig. 9 (a) Physical domain for the dusty gas flow in a converging-diverging nozzle;(b) Volume Fraction contours and (c) particle velocity vectors for dusty gas flow in a converging-diverging nozzle.





(b)
Fig. 10 Comparison of one-phase and two-phase gas Mach number distributions along the
(a) wall and (b) centerline of dusty flow in a converging-diverging nozzle.

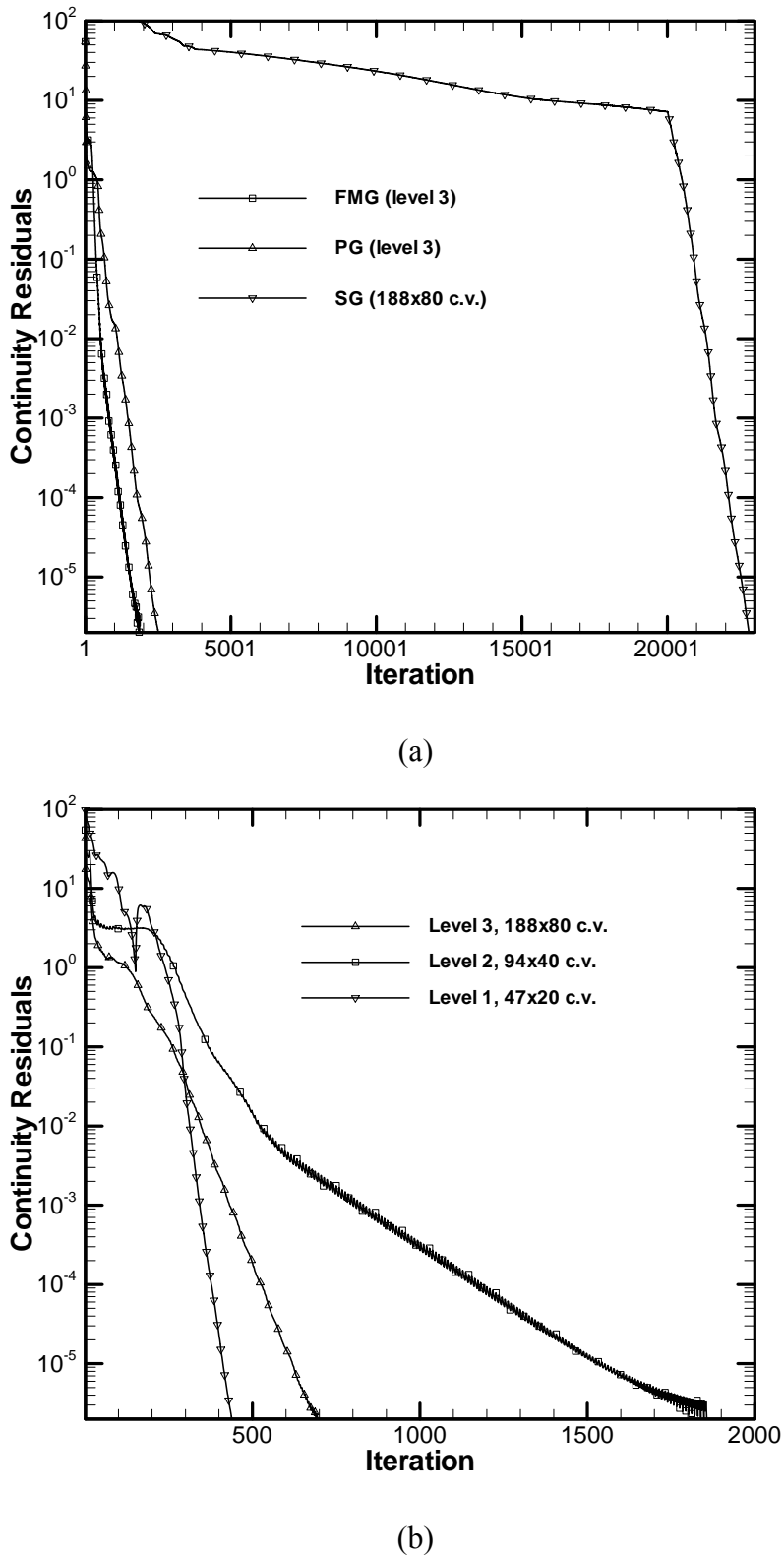


Fig. 11 (a) Mass residual history plots for the FMG, PG, and SG methods on the finest mesh for compressible dusty flow in a converging-diverging nozzle;

(b) Mass residual history plots for the FMG method on the various levels for compressible dusty in a converging-diverging nozzle.